

Master of Science Thesis

---

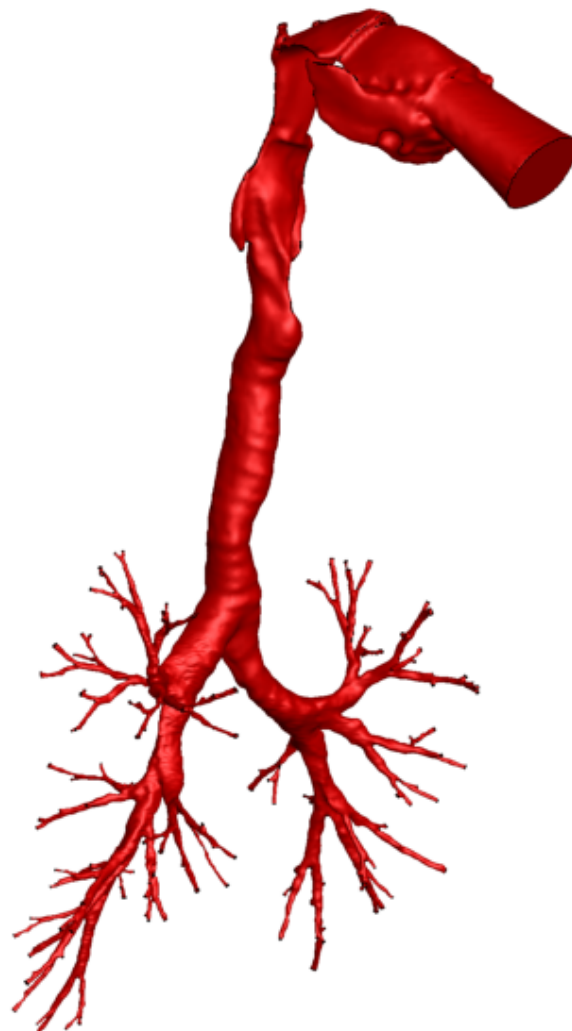
# Simulation of airflow in a realistic CT-scan derived lung geometry

---

W.H.K. Van Deun

---

February 17, 2011



# **Simulation of airflow in a realistic CT-scan derived lung geometry**

Master of Science Thesis

For obtaining the degree of Master of Science in Aerospace Engineering at Delft  
University of Technology

W.H.K. Van Deun

February 17, 2011



**Delft University of Technology**

Copyright © Aerospace Engineering, Delft University of Technology  
All rights reserved.

DELFT UNIVERSITY OF TECHNOLOGY  
DEPARTMENT OF AERODYNAMICS

Supervisor:

*prof. dr. ir. drs. H. Bijl*

Graduation committee:

*prof. dr. ir. drs. H. Bijl*  
*prof. dr. ir. C. Lacor\**  
*ir. V. Agnihotri\**  
*dr. ir. A.H. van Zuijlen*

(\* Vrije Universiteit Brussel (VUB), Department of Mechanical Engineering, Research Group Fluid Mechanics and Thermodynamics, Pleinlaan 2, 1050 Brussels, Belgium.)

February 17, 2011



## Abstract

Nowadays various studies utilizing computational techniques are trying to contribute to the medical world. In this light Computational Fluid Dynamics (CFD) techniques are already used for some time to simulate flow behavior in the human airway system. This was mostly done for idealized and simplified airway models as it is only recently that truly realistic geometry models are made available. It is believed that improving CFD techniques with respect to these realistic lung geometries may improve medical practice and help lung surgeons.

In this thesis the Reynolds Averaged Navier Stokes (RANS) equations are used to simulate airflow in a realistic human airway model derived from Computed Tomography (CT) scan data ranging up to 7 generations. This is done for inhalation at three different breathing rates. Due to the transitional nature of the flow, the  $k-\omega$  SST model is chosen to predict turbulence. For solving the flow equations the Fine/Hexa software (Numeca, Brussels, Belgium) is employed.

As a result of the grid independence study a mesh of 5,230,000 computational cells is chosen for all simulations. Also a software comparison is performed to see which solver is more efficient in performing simulations on the realistic lung geometry. With regard to this the Fluent solver has proven to be most efficient solver. Furthermore, results of the simulations including important flow phenomena and total pressure drop are in accordance with the literature. The results for airway resistance and mass fractions of the different lung lobes are discussed. Also, in order to simulate a surgical intervention, computations have been performed on geometries with lung lobes removed.

In order to have an effective CFD tool that can benefit the work of lung surgeons, still a significant amount of work needs to be done. The findings described in this paper are just a precursor.

## Acknowledgement

Writing these last words of my thesis I have come to realize that yet another year has passed. Looking back, it has been a really interesting and experienced journey for me. I think it is a good thing for every person to have a sense of variation in his life. I, for example, was excited to have a new working environment and to work on a subject with a slightly different application than what I was used to in Delft. I am talking about the shift from airplanes to lungs. In the past it has not always been easy to explain to others what I was doing. People always thought I would be an astronaut. But now having to explain that I am working with human lungs, I completely lost everybody.

First of all I am very grateful to Chris Lacor for giving me the opportunity to carry out this thesis at the VUB in Brussels and for always pushing me forward. This thesis could also not have been possible without the assistance of Hester Bijl. In this way I would like to express my sincere gratitude to her for the various pieces of advice and guidance and for always telling me to keep my focus on the goal. Because of the distance our communication was not always easy, but in the end we made it work and that is all that matters.

The past year did not went without difficulties. Halfway the year I had some software problems and had to switch to a different software. Honestly I was a bit de-motivated at the time. But thanks to the love and advice of my dear colleagues: Willem Deconinck, Vivek Agnihotri, Matteo Parsani, Florian Krause and my supervisor Chris Lacor, I was back on track. To this extend I would like to thank Willem Deconinck for his support during the old school days, when I was still working with the COOLFluid software. I wish him to best of luck with developing a better and more user friendly version of the software. Furthermore, I would like to thank all the other guys in the department for the nice coffee breaks and especially Allen Wery for his everlasting patience and assistance in times ruled by software problems.

A special word of gratitude goes to my personal supervisor, Vivek Agnihotri: Thanks for the numerous amounts of advice you have given me. I hope you will finally visit Antwerp one day, otherwise I will drag you there.

I would also like to thank my family for supporting me, all of my friends for those innumerable hours of inspiration at the bar, my bike "Black Beauty", which recently was stolen, for bringing me to the train station and everywhere else I needed to be and the NMBS for being always on time... NOT.

Last and most importantly I could not have done this without the love of my girlfriend, Isabelle. Thank you baby!

*February 1, 2011  
Willem Van Deun*

## Contents

Nomenclature .....	X
Introduction .....	XII
1. The human respiratory system .....	1
2. Literature Study .....	5
2.1. Background of the different airway models .....	5
2.2. Modeling methods for CFD .....	13
3. Airway Geometry .....	15
4. Mesh .....	17
5. Simulation model .....	20
5.1. Fluid model .....	20
5.2. Numerical Method .....	20
5.2.1. Reynolds Averaged Navier-Stokes equations .....	20
5.2.2. Turbulence model .....	21
5.2.3. Wall functions .....	22
5.2.4. Solver settings .....	23
5.3. Boundary conditions .....	25
5.3.1. Inlet .....	25
5.3.2. Outlet .....	25
5.3.3. Wall .....	26
6. Grid convergence Study .....	27
6.1. Introduction .....	27
6.2. Results .....	27
6.3. Conclusion .....	29
7. Results application I: The simplified geometry .....	30
7.1. Numerical Methods .....	30
7.2. Geometry of the model .....	30
7.3. Experimental set-up .....	31
7.4. Mesh .....	32
7.5. Results .....	32
7.5.1. Velocity and turbulent kinetic energy .....	32
7.5.2. Experimental validation .....	34
7.5.3. Conclusion .....	34
8. Results application II: The realistic geometry .....	36

8.1. Visualization of the results .....	36
8.2. Full geometry.....	38
8.2.1. Velocity .....	38
8.2.2. Turbulent kinetic energy.....	42
8.2.3. Pressure .....	43
8.2.4. Resistance .....	44
8.3. Geometry with lungs removed.....	45
8.3.1. Mass fractions.....	46
8.3.2. Pressure .....	48
8.4. Conclusion.....	48
9. Results application III: Software comparison .....	49
10. Conclusions and recommendations.....	51
Bibliography .....	52

## Nomenclature

### Greek symbols

$\varepsilon$	turbulent dissipation rate
$\varepsilon_{\text{rms}}$	root mean square error
$\sigma_k$	turbulent Prandtl number for $k$
$\sigma_\omega$	turbulent Prandtl number for $\omega$
$\rho$	air density
$\kappa$	von Karman constant
$\tau_{\text{wall}}$	wall shear stress
$\tau_{ij}^R$	Reynolds stress tensor
$\Gamma^{-1}$	preconditioning matrix
$\mu_t$	turbulent eddy viscosity
$\nu$	kinematic viscosity
$\omega$	specific turbulent dissipation rate
$\omega^+$	non dimensional form of $\omega$

### Roman symbols

A	inlet area
B	empirical constant
$D_h$	hydraulic diameter
E	energy
$E_g$	total gauge energy
$\vec{F}$	inviscid flux
$F_s$	safety factor
$\vec{G}$	viscous flux
$I_{\text{inlet}}$	turbulent intensity
$N$	grid size
P	perimeter
$P - P_{\text{in}}$	pressure drop
R	resistance
$Re_D$	flow Reynolds number based on the inlet diameter
T	time interval
$T_{\text{ref}}$	reference temperature
U	set of conservative variables
$U_{\text{loc}}$	local velocity
$U_{\text{ref}}$	reference velocity, taken as inlet velocity
V	control volume
$c_\mu$	constant, equal to 0.09
$k$	turbulent kinetic energy
$l$	turbulent length scale
$\dot{m}$	mass flow rate
$\dot{m}/\dot{m}_{\text{in}}$	mass fraction percentage
$p$	order of convergence
$\bar{p}$	mean pressure
$p_{\text{ref}}$	reference pressure

$p_g$	gauge pressure
$r$	grid refinement factor
$u$	velocity component in the x-direction
$u^+$	dimensionless velocity
$u_i$	instantaneous velocity components
$u'_i$	fluctuating velocity components
$\bar{u}_i$	mean velocity components
$u_\tau$	friction velocity
$v$	velocity component in the y-direction
$w$	velocity component in the z-direction
$y^+$	dimensionless normal distance from the wall
$y_{wall}$	distance from the wall

## Abbreviations

CFD	Computational Fluid Dynamics
CFL	Courant Friedrichs Lewy
COPD	Chronic Obstructive Pulmonary Disease
CT	Computed Tomography
DNS	Direct Numerical Simulation
FRC	Functional Residual Capacity
GCI	Grid Convergence Index
HRCT	High Resolution Computed Tomography
LES	Large Eddy Simulation
LLL	Left Lower lung Lobe
LUL	Left Upper lung Lobe
MDCT	Multi-Detector row Computed Tomography
MRI	Magnetic Resonance Imaging
PDI	Phase Doppler Interferometry
PIV	particle image velocimetry
RANS	Reynolds Averaged Navier Stokes
RLL	Right Lower lung Lobe
RML	Right Middle lung Lobe
RMS	Root Mean Square
RUL	Right Upper lung Lobe
SST	Shear Stress Transport
TLC	Total Lung Capacity
UZA	Universitair Ziekenhuis Antwerpen

## Introduction

Computational Fluid Dynamics (CFD) techniques are used more frequently in medical applications these days. They may provide valuable information and even lead to more effective treatments or methods. Therefore already some studies have started to translate findings from computer models to clinical applications, e.g. (Vos, et al., 2007). With respect to the airway system, CFD models have already been proven to predict the effect of an upper airway intervention in a number of ways, i.e. in terms of mass flow distribution, pressure drop, local airway resistance, etc....

However, in order to be of any use in the medical sector, CFD results have to provide a good approximation of reality in a reasonable time span. This means that the model and mesh generation, the time to reach a steady state solution and the time required to post process the result will have to be optimal for an effective use. It is therefore worthwhile to further develop CFD techniques with application in the human respiratory system (De Backer, et al., 2008).

The main question is then whether CFD techniques can be used to provide useful information with relation to a surgical intervention in the lungs, benefitting the work of lung surgeons. In order to try formulating an answer to this, two relevant questions will be answered in this thesis. Namely whether it is possible to find a mesh independent solution for a realistic lung geometry. Successively which software solver is then more effective in providing results.

Therefore, in the present study CFD simulations are performed on a truly realistic lung geometry extracted from Computed Tomography (CT) scan data. After performing these simulations also sections of the lung geometry will be left out to simulate surgery of the lungs and to monitor the resulting pressure drop and airway resistance. Keep in mind that the current geometry is state of the art and CFD simulations in the past were mostly done on simplified and idealized lung models.

In order to simulate the flow physics in the realistic airway model, use will be made of the commercially available Fine/Hexa software (Numeca, Brussels, Belgium), which will be compared with a different solver, namely Fluent (Ansys, Canonsburg, PA). It must be noted that in the past computations were already performed by De Geeter (2010) on the same geometry with Fluent. Furthermore, results obtained for the realistic geometry will also be compared with the results of De Geeter (2010) and with results from the literature where possible.

The first chapter provides a background of the working principle of the human respiratory system together with a description of the different biological parts. The literature study, as depicted in Chapter 2, gives an extensive summary of the various tested lung geometry models ranging from simplified to realistic. Also the different CFD techniques relevant to this thesis are discussed here.

Chapter 3 and 4 respectively give a detailed description of the realistic lung geometry and mesh. These chapters discuss how the geometry is obtained from CT scanning and further how it is captured with a computational mesh, describing its features. In Chapter 5 the complete simulation model is defined, ranging from the governing equations to the solver settings and boundary conditions used along the geometry.

The next chapters will deal with the results. Chapter 6 offers information about the mesh generation and the results of the grid independence study. Then a first validation of the Fine/Hexa solver on the simplified model is given in Chapter 7. The following chapters consider the realistic lung model. I.e. Chapter 8 offers the simulation results of the full lung model, as well as the results for the lung model with lobes removed. In Chapter 9 a comparison is performed with the Fluent solver. Consequently the conclusions are given in Chapter 10.

## 1. The human respiratory system

The respiratory system, which includes the airways, lungs and the respiratory muscles, is a biological system that is responsible for gas exchange. By breathing in, air and so oxygen is brought into the blood. The blood absorbs the oxygen and at the same time gives up carbon dioxide, which is carried out of the lungs by breathing out.

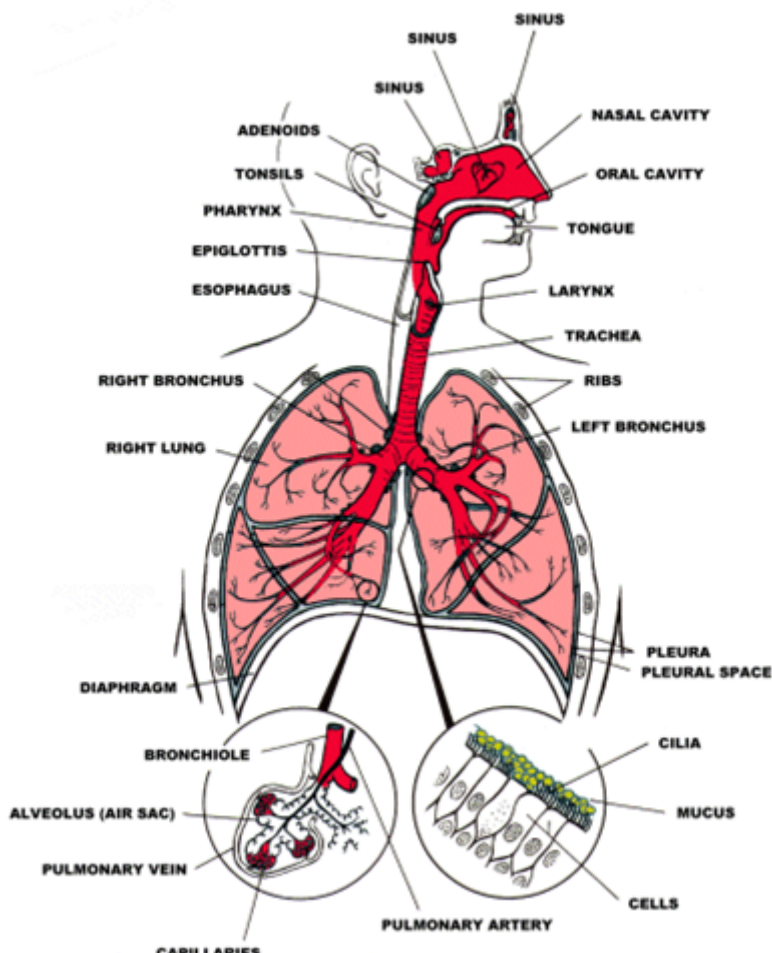


Figure 1.1: Schematic representation of the respiratory system<sup>1</sup>

The inhalation process is driven by the diaphragm, which is a sheet of internal muscle that extends across the bottom of the rib cage (see Figure 1.1) and supported by the external intercostal muscles. When it contracts, the content of the abdomen (body cavity) is pushed downwards and the thorax or ribcage expands. This creates a larger thoracic volume and consequently gives rise to an under pressure in the lungs with respect to the atmospheric pressure. Under this mechanism air will travel deeper into the lung.

Normal resting respirations are about 10 to 18 breaths per minute with a time period of 2 seconds. Each breath has a volume of about 500ml. During heavy inhalation (at rates exceeding 35 breaths per minute) accessory and intercostal muscles of respiration come into play and further expand the thoracic volume. The lungs are elastic by nature and during the inhalation process, the air is pushed

<sup>1</sup> Picture obtained from [https://www.lung.ca/children/grades7\\_12/respiratory/respiratory\\_system.html](https://www.lung.ca/children/grades7_12/respiratory/respiratory_system.html)

outwards until the pressure in the thorax reaches equilibrium with the atmospheric pressure. The exhalation is generally a passive process. In the case of forced exhalation, as when blowing out a candle, the expiratory muscles including the internal intercostal and abdominal muscles force the air to flow out.

As already mentioned, the major function of the respiratory system is gas exchange between the external environment and an organism's circulatory system. Upon inhalation, gas exchange occurs at the level of the alveoli, the tiny sacs which are the basic functional component of the lungs. Here the oxygen is attached to the hemoglobin molecules in the blood. Furthermore, in the alveolar region molecules of oxygen and carbon dioxide are passively exchanged by means of diffusion between the gaseous external environment and the blood.

The human respiratory tract is basically divided into three regions namely the extra-thoracic region, the tracheobronchial region and the alveolar region. The first mentioned region is the most relevant one considering the flow properties and will be discussed more extensively.

### ***Extra-thoracic region***

The extra-thoracic region consists of the nasal cavity, the mouth cavity, pharynx, larynx and trachea (see Figure 1.2). This region is most often referred to as the upper airway region or the nose, mouth and throat region.

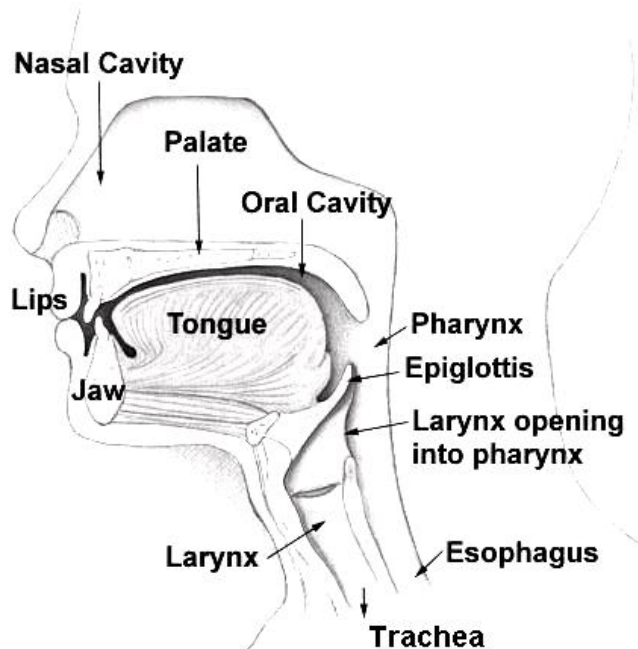


Figure 1.2: schematic representation of upper airway system (Finlay, 2001)

The nose is usually the preferred entrance for outside air into the respiratory tract. The nasal cavities, which are open spaces in the nose, act as a filter of foreign material, as a moistener and warm up the air before intake. In case of filtering, it are the hairs in the nostrils which filter out the foreign particles. Furthermore, the mucus and cilia in the nasal cavity collect dust, bacteria and other particles.

The other opening to the respiratory tract, the mouth also moistens and heats up the air but to a lesser degree than the nose. This is because air travels a lot faster through the mouth. The mouth may be the preferred passage for people who have a mouth-breathing habit or when suffering from

a cold or when performing a heavy exercise. The shape of the mouth cavity is a function of the position of the tongue and jaws. The roof of the mouth consists of the hard and soft palate followed by the uvula from where air flows into the oropharynx, which is connected with the nose through the nasopharynx (see Figure 1.3).

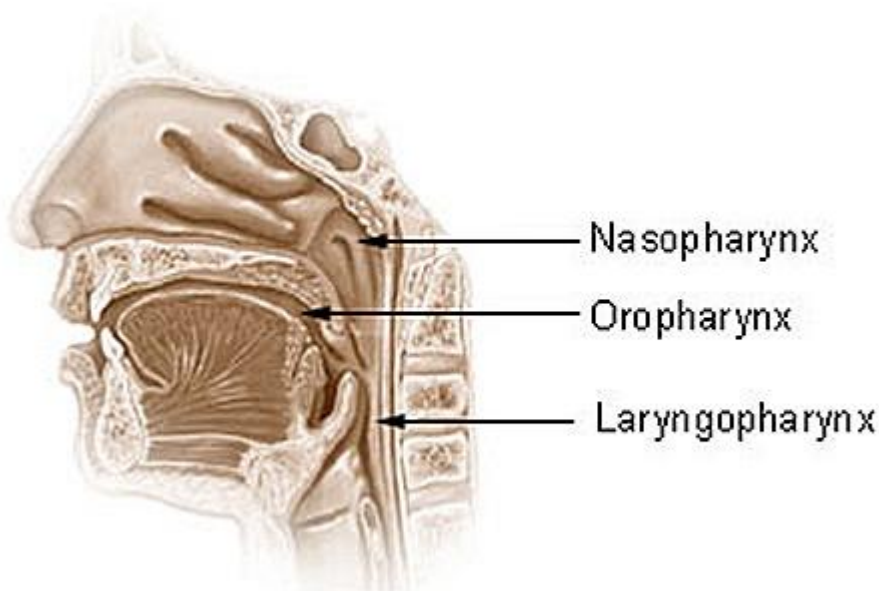


Figure 1.3: The larynx<sup>2</sup>

The oropharynx extends from the uvula to the epiglottis, which guards the entrance to the trachea. It has the function to block the trachea when food is swallowed, so that the food can be directed towards the stomach instead of the airway. Furthermore, air coming from the oropharynx travels through the laryngopharynx, which extends the flow to the larynx. The laryngopharynx together with oro - and nasopharynx form the pharynx, which has as function to collect the flow from nose and mouth.

The larynx or glottis is a complex structure, it consists of an outer casing of nine cartilages connected by each other by muscles and ligaments. The largest and best known cartilage is the Adam's Apple. The before mentioned epiglottis is also one of these nine cartilages. The larynx also contains the vocal chords. Speech is produced by letting the vocal chords vibrate with the moving airflow. When the amplitude of vibration gets higher the sound will be louder. The glottis width and area varies with the breathing cycle.

The trachea or windpipe, which acts as a passage to the lungs, is connected to the larynx. The trachea is a tube-like structure of approximately 10-14 cm long and 16-20 mm wide and is kept open by cartilage rings. The presence of these rings in the trachea wall can have a considerable effect on the flow dynamics. Similar to the nasal cavity the trachea has a protective function in the form of a filter through cilia on the walls. These cilia extend to approximately 5-10  $\mu\text{m}$  from the wall.

### ***Tracheobronchial region***

Furthermore, the trachea leads down to the thoracic cavity where it is split up into two cartilage-ringed and ciliated tubes called the right and left bronchus. Both have different sizes due to the

<sup>2</sup> Picture obtained from <http://distractible.org/2007/10/22/physical-exam-the-fair-inks>

position of the heart, which is situated more to the left side of the chest. The bronchi enter the lungs and spread into a kind of tree structure of primary, secondary and tertiary subdivisions ending up becoming tiny terminal bronchioles. The air path followed from the trachea into these bronchioles is known as the tracheobronchial region, which is also referred to as the lower airways.

### ***Alveolar region***

These bronchioles finally lead to the respiratory zone of the lungs, which consists of respiratory bronchioles, alveolar ducts and the alveoli, where finally the gas exchange finds place. These alveoli are one cell thick and are moist and thin. It is estimated that lungs contain about 300 million alveoli. This region is referred to as the Alveolar region<sup>3</sup>.

---

<sup>3</sup> Information about the respiratory system was obtained from the PhD theses of Brouns and Jayaraju and from [http://en.wikipedia.org/wiki/Respiratory\\_system#Physiology\\_in\\_mammals](http://en.wikipedia.org/wiki/Respiratory_system#Physiology_in_mammals).

## 2. Literature Study

### 2.1. Background of the different airway models

In the past various researchers have addressed parts of the lung geometry in order to study and understand its flow properties. In this chapter the most important publications are summarized and briefly discussed in order to have a clear view of the progress in this field. As previously mentioned the slow, normal and heavy breathing rates are about 15, 30 and 60 L/min respectively. These breathing rates are maintained as inlet condition in most of the publications given below. This makes that the relative flow Reynolds number for this research lies somewhere in the range of  $\sim 600$ -4000, varying with the inlet diameter.

This chapter will be split up into two parts. First the different airway models ranging up to the trachea (generation 0) are discussed (see Figure 2.8 for a clear picture of how the air pipe is divided into generations and bifurcations). In the second part the more relevant airway models containing more generations are discussed. In both cases also the corresponding flow characteristics are mentioned.

#### ***Geometries without generations and their corresponding flow characteristics***

It is known that the overall complexity of the upper airway path with its bends and varying cross-sections poses some severe geometry modeling difficulties both for experimental and computational studies. Therefore various degrees of geometrical complexity for the upper airway models have been employed. In this section the different employed airway geometries with corresponding flow patterns as observed by various researchers are presented from simplest to more complex.

Katz and Martonen (Katz, et al., 1996) performed preliminary flow studies using a finite element analysis and created for this purpose a simple 3D model of the larynx (see Figure 2.1). The model was based on morphometric measurements of replica human casts and Weibel's morphology of the tracheal dimensions. In this case the larynx was modeled as a six cm long cylinder which has at its entrance and exit area a circular cross-section. Furthermore, the gaps created by ventricular and vocal cords were taken to be ellipses. Using this model they tried to understand basic flow patterns at three different flow rates: 15 (slow breathing), 30 (normal breathing) and 60 l/min (heavy breathing). It was observed that due to the changes in cross-sectional area there exists a swirling circumferential flow through the larynx.

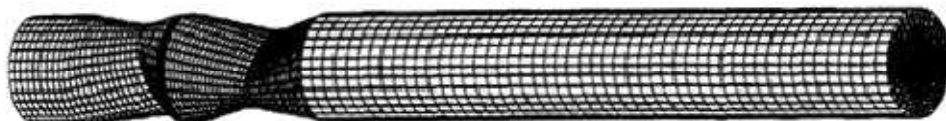


Figure 2.1: simplified 3D model of larynx as developed by Katz and Martonen

Katz et al. (Katz, et al., 1997) broadened this work and used the same model as described above to study the influence of the glottal aperture on the flow pressure and velocity distributions. It was found that the complex geometry produces jets, recirculation zones and circumferential flows. For example Figure 2.2 shows the recirculation zones as formed by the different flow rates due the shape of the larynx.

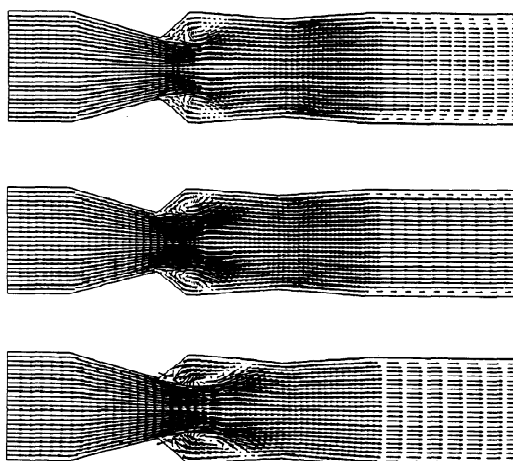


Figure 2.2: Lengthwise velocity vector lines for flow rates of 15, 30 and 60 l/min respectively

Corcoran and Chigier (Corcoran, et al., 2000) used Phase Doppler Interferometry (PDI) in a cadaver based larynx-trachea model to measure the axial velocity and turbulence intensity. This was done for three different flow rates representing quiet and normal breathing. As model they used a polyurethane casting of the human larynx connected to a glass tube with an inside diameter matching the tracheal diameter of the cadaver. For this model high levels of axial turbulence intensity were noted near the anterior and left tracheal walls within two tracheal diameters. An additional observation was that the average turbulence intensity at a lower flow rate was 20% higher than at a higher flow rate. Furthermore, at all three flow rates, reverse flows with large velocities were observed in the anterior part of the trachea and a tracheal jet occurred at the posterior side of the trachea.

As is seen in the previously discussed airway models, the pharynx and larynx region were always modeled with a constant cross-section. Also the total region of pharynx, larynx and oral cavity was normally modeled with a 90° curved bend. But Li et al. (Li, et al., 2007) and Cheng et al. (Cheng, et al., 1999) have shown that such a basic and simplified model can give rise to large errors when compared to measured data obtained with cast replicas.

Therefore in the study of Zhang et al. (Zhang, et al., 2002) , where the focus is on the laminar-to-turbulent airflow regions for the three typical flow rates (15, 30 and 60 l/min), the aim was to develop a relatively simple but more representative oral airway geometry, consisting of the mouth, pharynx, larynx and trachea (Figure 2.3) The new surrogate geometry consists of variable circular cross-sections and as suggested by Cheng et al. (Cheng, et al., 1999) the mouth, pharynx and larynx region were modeled as a near 180° curved bend. The dimensions of cross-sections are based on data from a replicate human oral airway cast of a healthy male adult as provided by Cheng et al. It was observed that for normal breathing the velocity profiles were seen to become somewhat skewed in the curved part of the oral cavity and the pharynx-larynx region due to centrifugal forces (see left part of Figure 2.4). Furthermore, flow separation was seen to occur due to the abrupt geometric changes and an asymmetric laryngeal jet appeared after the glottis area. The right part of Figure 2.4 gives the distribution of the turbulent kinetic energy across the upper airway system.

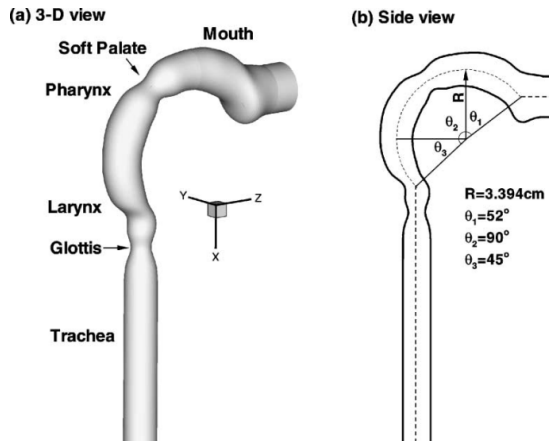


Figure 2.3: More representative 3D geometry of the mouth-throat model as developed by Zhang et al.

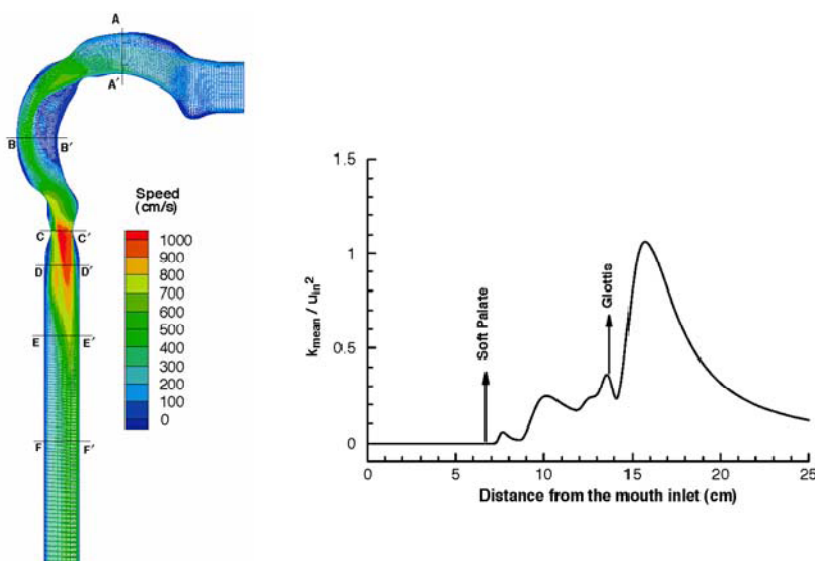


Figure 2.4: (left): Mid-plane velocity contours; (right): Variations of cross-sectional are-averaged turbulent kinetic energy in upper airway model developed by Zhang et al.

Stapleton et al. (Stapleton, et al., 2000) created with the aid of data from computed tomography (CT) scans, MRI scans and direct observation of living subjects an ‘average’ idealized geometrical model of the extra-thoracic airway. It can be seen from Figure 2.5 that this model exists of simple geometric shapes. Compared to using a model based on an airway cast, this approach has no need for high grid resolutions at the walls the resolve small airway irregularities. However, a drawback is that the oral cavity is too simplistically modeled.

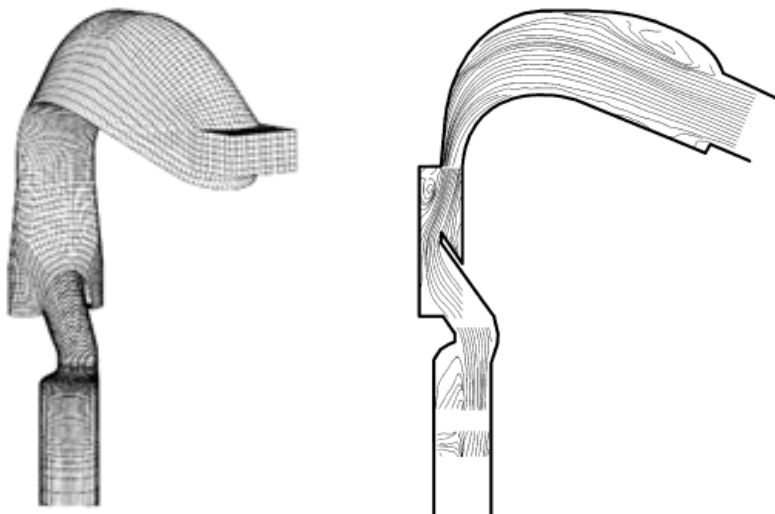


Figure 2.5: (left) idealized geometrical model of the extra-thoracic airway as developed by Stapleton et al. (right) 2D streak lines from PIV at a normal inhalation flow rate of 30 l/min (Heenan, et al., 2003)

Johnstone et al. (Johnstone, et al., 2004) also used the airway model of Stapleton et al. (Stapleton, et al., 2000) to study experimentally with hot wire anemometry the mean and RMS axial velocity field in the central sagittal plane during various steady flow rates. As can be seen from the right part of Figure 2.5, regions of separated and recirculating flow are located downstream of the mouth inlet, uvula and larynx. Also circumferential secondary flow patterns have been spotted in the oral cavity. Furthermore, the normalized hot-wire axial velocity profiles ranging from the oral cavity to the oropharynx were found to increase as the Reynolds number decreases. This points out the presence of stronger viscous effects at lower inhalation flow rates.

Yu et al. (Yu, et al., 1998) constructed a more complete model of the upper airway including the nasal and oral cavity, pharynx, larynx, trachea and first two generations of the tracheobronchial tree. It was created with the aid of a simplified teaching model used by the medical school. There are, however, some shortcomings including an incorrect duplication of the exact nasal morphology and a too simplistic representation of the oral airway. Furthermore, the first two bifurcations and the trachea were modeled as constant cross-sectional circular tubes. When considering the results, it can be seen that the different inhalation patterns, i.e. nasal inhalation, oral inhalation or combined inhalation have a significant effect on the velocity profiles within the laryngeal airways. Also because of its complex shape, the larynx is considered to be the key morphological factor affecting the airflow characteristics in the upper airway system.

At this moment the need for a more realistic representation of the upper airway is recognized. In this aspect, Brouns et al. (Brouns, et al., 2007) derived from available CT-scan data a simplified and smoothed yet realistic human upper airway geometry by using preliminary CFD-simulations. In this way the critical features of the flow field are preserved, as can be seen from the left part of Figure 2.7. Most physical features, like the shape of the mouth cavity, position of the trachea and the epiglottis are maintained in the simplification.

Xi and Longest (Xi, et al., 2007) compared in this case the micro-particle deposition of the CT based realistic mouth-throat model against the simplified model from Brouns et al. (2007). It was concluded that the realistic geometry provides the best predictions for the regional particle deposition in comparison to experimental data.

As a consequence Jayaraju et al. (Jayaraju, et al., 2007) performed RANS simulations on a truly realistic upper airway model obtained from CT scan data (see Figure 2.6).

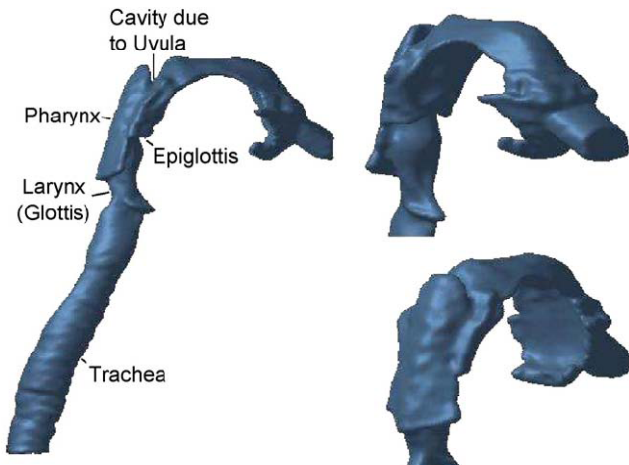


Figure 2.6: 3D mouth-throat model as extracted from CT scan data

They concluded that a major amplification in kinetic energy takes place downstream of the larynx and that velocity profiles were seen to become skewed in the curved portions of the oral cavity, pharynx and larynx. Furthermore, it was stated that quickly after the larynx, the skewness of the velocity profile as well as the strength of the recirculation zone vary with the given airway model. In conclusion, pharynx as well as larynx should be considered as key morphological factors affecting the flow characteristics. In Figure 2.7 the results of Brouns et al. (2007) and Jayaraju et al. (2007) are compared.

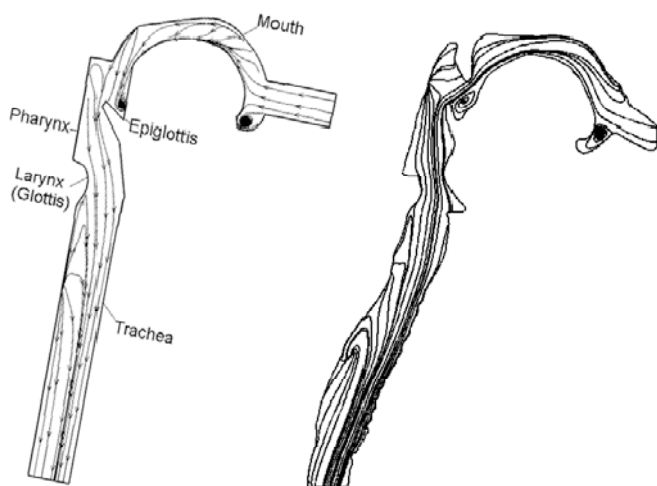


Figure 2.7: (left): Mid-plane velocity vector lines at normal breathing rate in a simplified model as obtained by Brouns et al. and (right): a realistic model as used by Jayaraju et al.

### **Geometries with more generations**

Previous described models all extend from the mouth cavity down to the trachea (also referred to as generation 0). Figure 2.8 describes how the airway is split up into generations (gen) and bifurcations (Bif.). It is stated that a realistic physical geometry, incorporating a large number of generations, is essential for adequately simulating fluid dynamics in human airway systems. It is due to the complexity of the human tracheobronchial tree, that simulations are limited to small parts of the

respiratory tract. In this section diverse lung models that take more generations into account are discussed ranging from idealized to anatomically correct geometries.

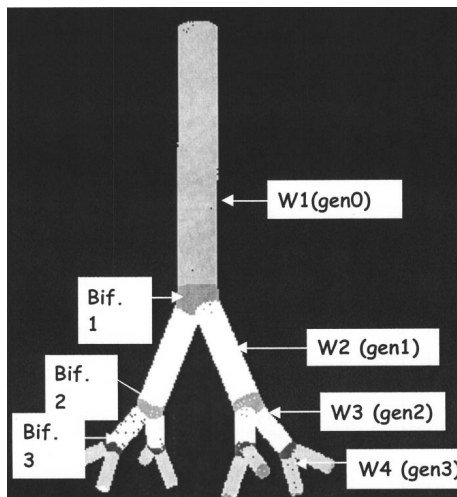


Figure 2.8: Computational domain is divided into bifurcations and generations (from Nowak et al. (2003))

One of the first and most widely adapted models for CFD simulations that takes more generations into account is characterized by a regular, symmetric and dichotomous (i.e. splitting up in pairs) branching pattern. This model for the airway geometry has its origin in the so-called trumpet model of Weibel (Weibel, 1963), who measured the dimensions of airway branches of a human lung up till generation G4. After this his measurements were taken to be less complete down to generation G10, where only 10% of the branches were measured. It is stated that the absence of airway curvature and surface irregularities make the flow fields in a Weibel-based model very different from those in a real lung. Many past articles have made use of idealized cylindrical branching geometries over a few generations. For example Liu et al. (Liu, et al., 2003) studied the 3D inspiratory flow in a third generation asymmetric model with the 5<sup>th</sup> till the 11<sup>th</sup> branch of Weibel's B model. Nowak et al. (Nowak, et al., 2003) used data from CT scans, although only down the 4<sup>th</sup> generation subunit, to characterize the airway system more realistically. They compared a realistic model based on a CT scan with a 3.5 generation subunit model based on the Weibel model A, where each generation subunit consists of 3 generations (see Figure 2.9). Dividing in subunits is done in order to realize the simulation of smaller sections of airways and to minimize memory requirements. They concluded that a simulated Weibel-based model does not provide accurate results compared to simulations performed on a real CT scan based geometry.

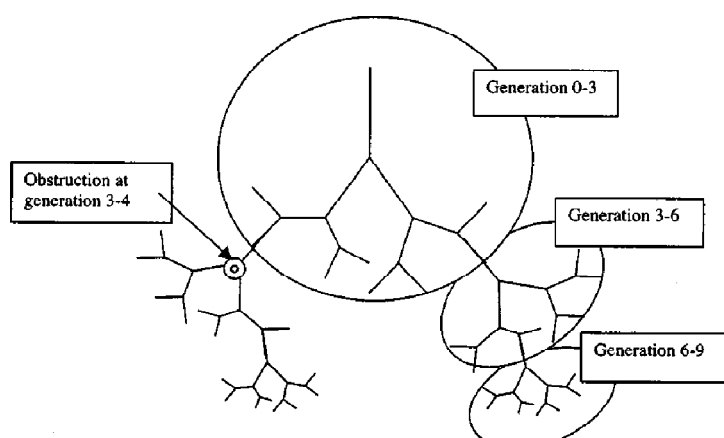


Figure 2.9: Schematic of three levels of 3.5 generation sub-units

Similarly Zhang and Kleinstreuer (Zhang, et al., 2004) looked at the transient flow effects in a human upper airway model consisting of two connected segments of a simplified human cast replica. The first one extending from the mouth to generation G0 (trachea) and the second one continuing with symmetric bifurcations over generations G0 to G3, based on Weibel's model. They used 420,000 computational cells for the first segment up to G0 and 670,000 cells for the four-generation (G0, G1, G2 and G3) airway model.

In an attempt to perform numerical simulations through a more extensive geometry Calay et al. (Calay, et al., 2002) studied the respiratory flow patterns in a single first-generation bifurcation, following only one bifurcation, and in a multiple-bifurcation model using three generations as based on the anatomy given by Horsfield et al. (Horsfield, et al., 1971). They used four different grid densities consisting of 31,104; 79,820; 159,872 and 320,980 nodes. Van Ertbruggen et al. (van Ertbruggen, et al., 2005) also used the morphometrical data of Horsfield et al. (1971) to study the gas flow in a realistic 3D model of the bronchial tree, starting from the trachea using seven generations. While these studies present a more extensive estimation of airflow behavior in the lungs, they still rely on an idealized smooth representation of the airway geometry.

For this reason Cebral and summer (Cebral, et al., 2004) and also Nowak et al. (2003) used CT scan data to characterize the tracheobronchial region more realistically. Cebral and Summer (2004) studied the airway tree down to four generations using a virtual bronchoscopy reconstruction method. Airflow patterns were simulated computationally in generations ranging from G0 to G4.

Other realistic anatomical models have been created based on mathematical algorithms and new experimental imaging techniques. For example Schmidt et al. (Schmidt, et al., 2004) developed an airway model containing 17 generations. This model is derived from High-Resolution Computer Tomography (HRCT) imaging of an in vitro preparation.

Gemci et al. (Gemci, et al., 2008) studied the airflow and pressure drop using the digital reference model developed by Schmidt et al. (2004) of the 17 generations airway model containing 1453 branches. They didn't choose the model of Spencer et al. (2001) although this model includes up to 23 of the 26 generations of the human tracheobronchial airways. This was due the lack of anatomical detail and accuracy in comparison with the 17-generation model developed by Schmidt et al. (2004). For this case specially adapted image processing algorithms were applied to delineate and segment the bronchi. Furthermore, the mouth and glottis have not been included in the model, because the authors expect that this exclusion will not have a direct effect upon the downstream flow as there is a gradual pressure recovery at the distal end of the trachea (Ma, et al., 2006). More so the trachea appears to have negligible influence on the total lung resistance. The mesh of the lung model, which consists of 6,744,000 unstructured tetrahedral computational cells (of which 1,063,000 cells in the G0 zone and 5,680,000 cells in the remaining zones), represents the somewhat irregular but realistic asymmetrical branching patterns of the larger airways. It includes varied airway lengths and cross-sectional areas. As can be seen from the right part of Figure 2.10, a simplified tube-like surface representation is constructed from the topological representation.

Kriete et al. (Kriete, et al., 2004) studied the oxygen gas transport in a digital reference model also based on data by Schmidt et al. (2004) with a limited 29 terminal bronchi outlets, as opposed to Gemci et al. (2007) who include all 720 bronchi outlets. Their final mesh contained a total of 456,463 prism and tetrahedral elements using the ICEM CFD software package.

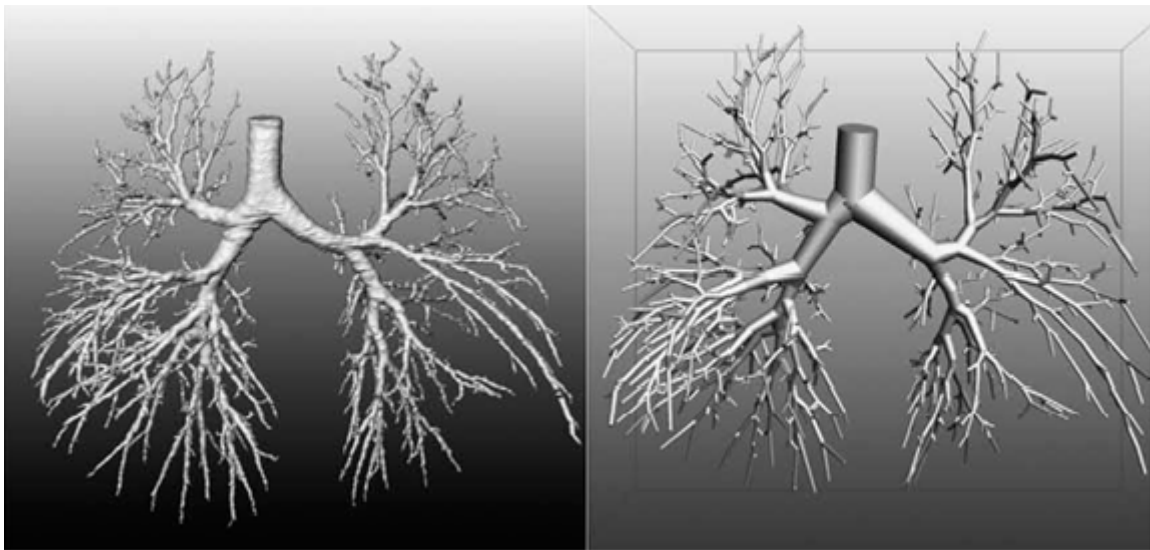


Figure 2.10: 3D visualization of bronchial tree models from Schmidt et al. (2004) (left): surface representation of segmented volume data; (right): visualization of a tube model reconstructed from abstracted topological graph data.

Considering the different mesh generation techniques available, Longest et al. (Longest, et al., 2007a) studied the effects of 4 different meshing techniques and the grid convergence on velocity fields and particle deposition patterns in two different bifurcating respiratory models, i.e. a single bifurcation model and a double bifurcation model. Accuracy of the simulations has been assessed by a comparison with experimental in vitro data available from the literature. Quantitative grid convergence was assessed based on a grid convergence index (GCI), which accounts for the degree of grid refinement. For all resolutions considered the unstructured tetrahedral mesh gained better results compared to the structured hexahedral mesh which has a GCI value one order of a magnitude lower. But as was also observed the hexahedral mesh style had reduced run times by a factor of 3.

As morphological irregularities show growing importance, the time for truly realistic image-based lower airway models has come. As previously mentioned, Cebral and summer (2004) and Nowak et al. (2003) already touched upon this topic. To further extent, Lin et al. (Lin, et al., 2007) numerically studied the importance of the upper and tracheobronchial airways and their role in determining central airflow patterns with particular attention paid to the importance of turbulence. They imaged volumetric scans of a volunteer using Multi-Detector row Computed Tomography (MDCT) to derive the geometry of the upper respiratory tract. In their study they made use of two geometries. Geometry 1 ranges from a mouth piece to the tracheobronchial tree including up to 6 generations, while geometry 2 only comprises the tracheobronchial airways. The mesh for case 1 contains 1,390,808 nodes and 7,115,300 tetrahedral elements, whereas the mesh for the second geometry has 454,165 nodes and 2,136,160 tetrahedral elements.

A more recent study by Lambert et al. (Lambert, et al., 2010) utilizes a real CT-based geometry of a human lung, which includes five distinct lung lobes, that was scanned at a total lung capacity of 85%. The airway model in this study also includes the upper airways and the central airways up to 7 generations. The computational domain was sub-divided into 65 sub-volumes with volume boundaries. Also two different mesh densities were constructed, the first one contained 899,465 nodes and 4,644,447 tetrahedral elements, while the second one contained 1,528,932 nodes and 8,063,559 tetrahedral elements.

Some of the previous studies already considered patient-specific geometries, resulting in more realistic flow behavior. De Backer et al. (De Backer, et al., 2008) stated that the absence of patient-specific boundary conditions (BC) still limits the reliability of CFD results for application in clinical

practice. Their study presents a patient-specific approach where both the geometry and BC's are based on individual imaging methods using CT. They assessed the internal flow distribution of a 73-year-old female suffering from chronic obstructive pulmonary disease (COPD). For the numerical simulation they used a inhalation flow rate of 23 l/min and assumed and almost laminar flow. Also the  $k-\varepsilon$  turbulence model is chosen to take some (small) turbulence effects into account.

## 2.2. Modeling methods for CFD

CFD numerically solves the Navier-Stokes equations which describes the flow behavior. It allows for the description of regional flow and pressure profiles in and around structures including anatomical ones. The amount of scientific papers describing the use of CFD for studying the flow behavior in the upper airways are growing rapidly. Different numerical methods are classified based on the nature of the flow, i.e. laminar, transitional or turbulent. This classification is important because when dealing with turbulent flows, the whole range of turbulence models and their ability to accurately predict the physics of turbulence comes into the picture.

There are a few regions of the respiratory system where the flow is predominantly laminar. Solving for laminar flow reduces the complexity of the simulations and increases the computational speed. The assumption of laminar flow in tubes and bifurcations, where the Reynolds numbers is only a few hundred, has been previously studied by many e.g. (Hofmann, et al., 1991) (Comer, et al., 2001) (Li, et al., 2007) (Kleinstreuer, et al., 2007).

As already stated before, depending on the breathing rate and inlet diameter, the Reynolds number ranges roughly from a few hundred to a few thousand, however. In this matter Stapleton et al. (2000) for example found that the flows in larynx and trachea are normally turbulent or at least transitional. This has as consequence that we have to be careful with the results obtained by assuming laminar flow in these regions.

### ***Reynolds Averaged Navier Stokes (RANS)***

Another option is to include turbulence and use the Reynolds Averaged Navier-Stokes (RANS) equations with the aid of a turbulence model such as  $k-\varepsilon$  or  $k-\omega$ . The required grid resolution is relatively small and therefore it is the most widely used approach for modeling turbulence. Using these two equation models, the turbulent flow features are modeled by solving the variables for turbulent kinetic energy ( $k$ ) and turbulent dissipation rate ( $\varepsilon$ ) or specific turbulent dissipation rate ( $\omega$ ). The specific dissipation rate can also be thought of as the ratio between  $k$  and  $\varepsilon$ .

Katz et al. (1996) used the standard  $k-\varepsilon$  model to understand the effect of flow rate on the flow patterns in a geometry based on laryngeal casts as described above (Figure 2.1). Stapleton et al. (2000) further tested the performance of this model in a mouth throat geometry at a turbulent flow rate of 28.3 l/min. However, when the results obtained with the  $k-\varepsilon$  model were compared with experiments, significant deviations were reported. Furthermore, other researchers, e.g. (Katz, et al., 1996) (Katz, et al., 1997) (Renotte, et al., 2000) (Gemci, et al., 2003) have studied flow patterns in the larynx utilizing this model.

It is noticed that the  $k-\varepsilon$  model has its shortcomings, which indicates the need for an experimentally validated low Reynolds number (LRN) turbulence model. A model that can represent laminar, transitional and turbulent flows in an upper airway model where realistic inhalation flow rates apply. On this matter Brouns et al. (2007) and others compared the  $k-\varepsilon$  model with the  $k-\omega$  model. They concluded that the velocity profiles in the trachea are best predicted by the latter one. In the

pharynx, however, the velocity profile of the pharyngeal jet differs from the measured profile, but it differs even more when the  $k$ - $\varepsilon$  model is applied.

The  $k$ - $\omega$  model has as advantage that it possesses a non-trivial solution for  $\omega$  as  $k$  goes to zero. It is thus expected to capture flow characteristics which a  $k$ - $\varepsilon$  model fails to handle. Considering this model, there are two main types, i.e. the standard and the Shear-Stress Transport (SST)  $k$ - $\omega$  model. It is known that SST model is more accurate and reliable compared to the standard model. The advantage of an SST  $k$ - $\omega$  model is that it can obtain an accurate laminar solution when the turbulent viscosity approaches zero. This is a necessity when dealing with flows in transitional regions. For example Zhang and Kleinstreuer (Zhang, et al., 2003) tested the performance of the LRN  $k$ - $\omega$  model of Wilcox (Wilcox, 1998) in a test channel with local constriction at a transitional Reynolds number of 2000. Their results showed good agreement with the experiments when comparing velocity and kinetic energy levels. Brouns et al. (2007) made an elaborate comparison between the different commercially available RANS turbulence models with experimental results at different sections in a realistic human upper airway model. They also concluded that the low Reynolds number SST  $k$ - $\omega$  model has the best prediction for the velocity profiles in the trachea. For high flow rates the kinetic energy is well predicted, but for lower flow rates the different turbulence models over predict the turbulent kinetic energy.

### ***Large Eddy Simulation (LES)***

Modeling technique using Large Eddy Simulation (LES) can also be used, for they are supposed to be more accurate, but also more time consuming. LES is a technique where the large energy carrying eddies are simulated, while the smaller eddies are filtered and modeled using a sub-grid scale model. It involves the use of a relatively fine mesh. Jayaraju et al. (2007) compared a RANS simulation using the SST  $k$ - $\omega$  model and a LES simulation in a CT scan extracted realistic geometry of the upper airway geometry (Figure 2.6). They concluded that LES results have similar velocity and kinetic energy profiles as compared to the experimental data, whereas RANS shows less accurate results.

In conclusion, use of RANS will be made for solving the flow equations as LES is considered too time consuming given the complexity of the realistic lung model. In addition, when taking into account the transitional nature of the flow regime in the trachea and larynx, the SST  $k$ - $\omega$  model offers the best turbulence prediction.

### 3. Airway Geometry

The airway model of a COPD patient was obtained from the UZA (Universitair Ziekenhuis Antwerpen). A COPD patient has bronchial carcinoma, which means a shortness of breath due to the narrowing of the airways most commonly from tobacco smoking, and will be treated with lobectomy (lobal removal). The UZA performed high resolution CT scans of the lungs at two different lung levels, namely the functional residual capacity (FRC) and total lung capacity (TLC), which provides a lot of additional information. The scanning equipment used is state-of-the-art such as the 64-slice GE light speed scanner, which allows for scanning of the lower airways in less than 10 seconds. Also bear in mind that at the moment of the scanning the patient is breathing through a mouthpiece.

The obtained information is then used to reconstruct the individual 5 lung lobes together with the airway tree. The right lung consists of 3 lobes: the right upper lobe (RUL), the right middle lobe (RML) and the right lower lobe (RLL), whereas the left lobe contains the left upper lobe (LUL) and the left lower lobe (LLL) (see Figure 3.1). The model for the airway tree reaches from the mouth to the larynx, the trachea and then down to the diaphragm and the first bifurcation (see Figure 3.2). Airways were reconstructed up to the minimum diameter where they could accurately be detected with the CT scan ( $\pm 1\text{mm}$ ). This led to the modeling of bifurcations up to the 7<sup>th</sup> generation. Furthermore, all reconstructions were done using the Mimics software package (Materialise NV, Leuven, Belgium). The mesh model was smoothed and cut at the inlet and outlet and made available in STL format (tri-based). This format can then be imported in the Hexpress Hybrid software (Numeca, Brussels, Belgium) for meshing purposes.

In CFD in order to have accurate computations it is a necessity to have case (here patient) specific boundary conditions. These conditions can equally be extracted from the scanning (De Backer, et al., 2008). The two CT scans (TLC and FRC) make it possible to assess the relative lung expansion and consequently the relative mass fractions going to their respective lobes can be determined.

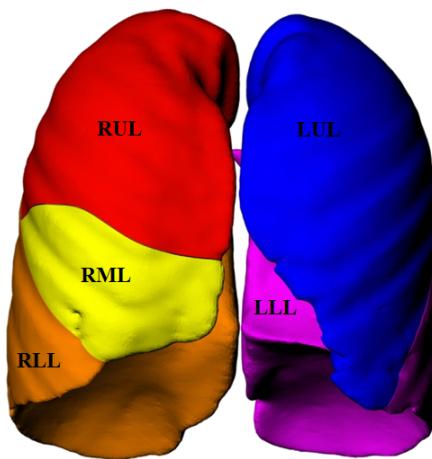


Figure 3.1: The five lungs lobes

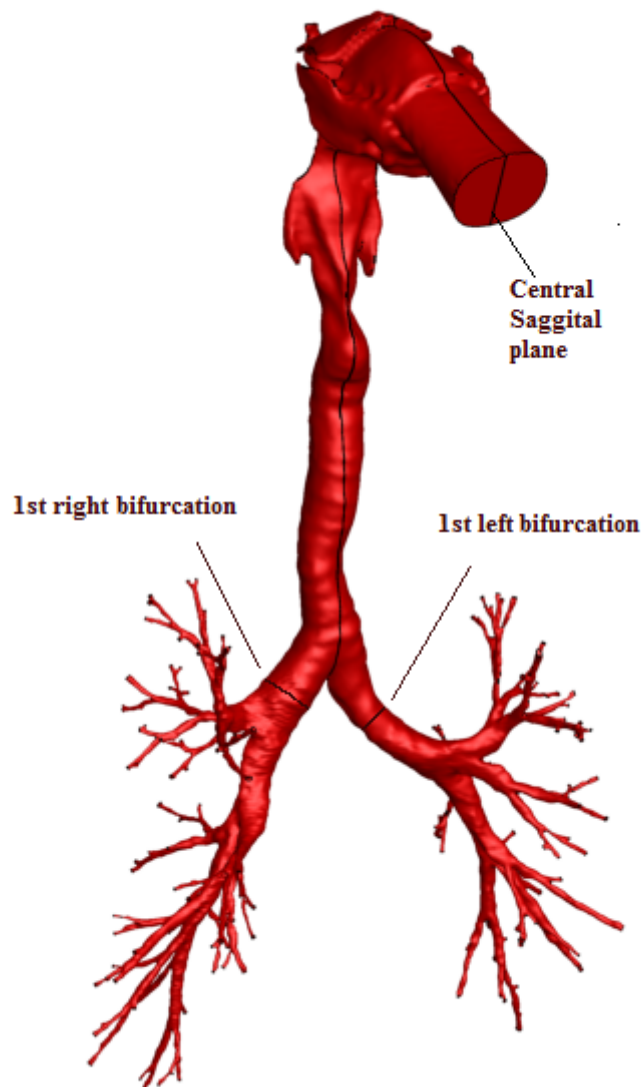


Figure 3.2: The realistic lung geometry with indication of three cutting planes

## 4. Mesh

In this chapter the computational mesh is depicted together with a description of its near wall behavior. It is important when using RANS to have a sufficient number of computational cells in the boundary layer. The different options for properly capturing the viscous layer are discussed in the near wall section.

The next step towards performing CFD simulations is to make a computational grid on the obtained airway geometry in which the mathematical flow equations can be solved. In principle there are two kinds of grids: namely structured and unstructured grids. The main advantage of structured grids is their ability to capture local gradients and provide at the same time an accurate solution. However, the construction of these grids is not always possible, especially with complex geometries. It is therefore advised with the present geometry in mind to resort to unstructured grids, which have an easier construction as advantage.

As will be explained in more detail in Chapter 6 of this thesis, CFD computations will be done on an unstructured hybrid mesh, which was created with the aid of the Hexpress Hybrid software (Numeca, Brussels, Belgium) and is depicted in Figure 4.1.

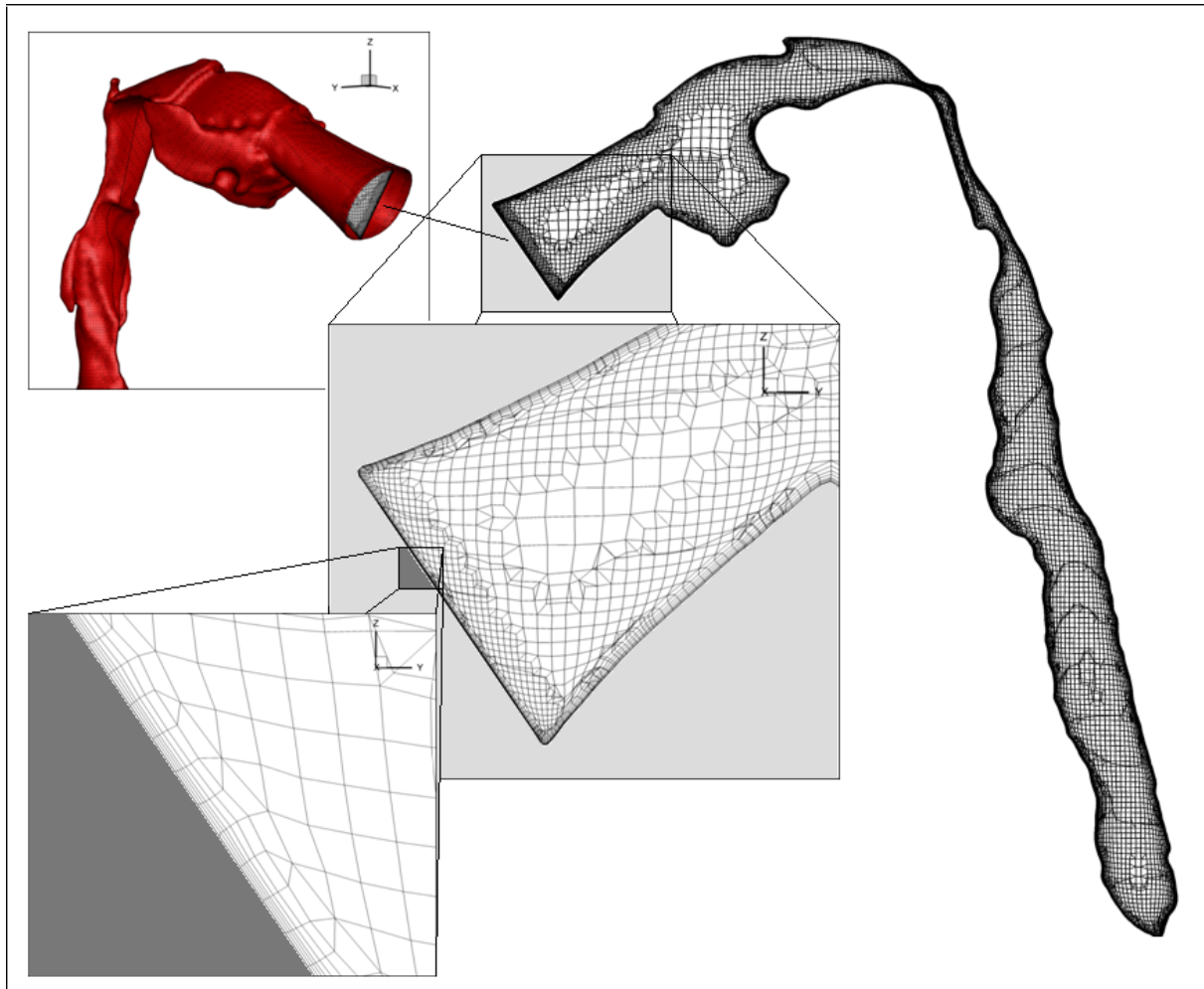


Figure 4.1: Visualization of the unstructured hybrid mesh of 5.23 million cells

### Near wall behavior

When computing turbulent quantities it is important to place the first grid node at a certain distance away from the wall boundary ( $y_{wall}$ ). In order to estimate an appropriate value for  $y_{wall}$ , the flow Reynolds number based on the wall variable  $y^+$  is calculated as in eq. (4.1). Here  $u_\tau$  signifies the friction velocity, defined in eq. (4.2).

$$y^+ = \frac{u_\tau y_{wall}}{v} \quad (4.1)$$

$$u_\tau = \sqrt{\frac{\tau_{wall}}{\rho}} \quad (4.2)$$

$\tau_{wall}$  being the wall shear stress and  $y^+$ , the dimensionless normal distance from the wall. Figure 4.2 shows the evolution of  $u^+$  against  $y^+$  (Lindgren, 1965). Here:

$$u^+ = \frac{\bar{u}}{u_\tau} \quad (4.3)$$

The flow equations are thus recast in non-dimensional form in order to derive solutions for the viscous and logarithmic layer. In our case we have smooth walls, which means the surface irregularities are submerged in the viscous sub-layer. Then the following linear relation, given by eq. (4.4), is valid for the viscous layer:

$$u^+ = y^+ \quad (4.4)$$

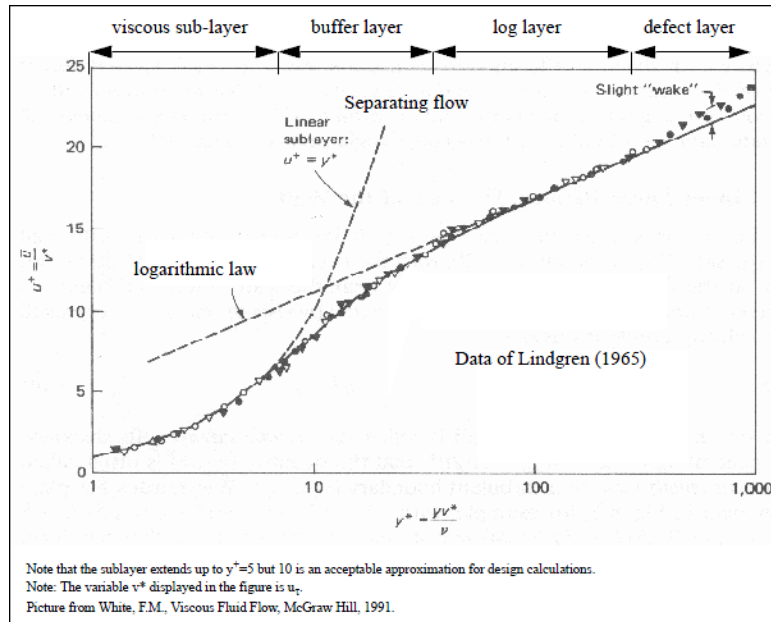
While in the logarithmic layer for a fully developed turbulent flow, we have the following relation with the experimentally fitted constants  $B$  usually taken as 5.36 and  $\kappa$ , the von Karman constant equal to 0.41:

$$u^+ = \frac{1}{\kappa} \ln(y^+) + B \quad (4.5)$$

In the intermediate buffer layer ( $5 < y^+ < 30$ ) neither of the above relations is valid and caution needs to be taken.

From here on a choice needs to be made between two distinct options in order to capture the physics of the near wall region for our complex geometry. The first one is to make a very fine mesh up against the wall, which is needed for wall integration in order to capture the high gradients and turbulence variables that exist in the viscous layer. Wall integration, which makes use of damping functions, requires that the first computational cell next to the wall is located within the viscous sub-layer, so that  $y^+ \cong 1$ . This approach requires a significant amount of computational cells in the boundary layer.

The second approach is to make use of wall functions, which are meant to circumvent the excessive grid requirements and allows for grids that are relatively coarse in the near wall region. Here the cell closest to the wall can be placed in the viscous layer, buffer region or in the logarithmic region (see Figure 4.2 for the different regions). In this way the number of cells in the boundary layer is reduced. Furthermore, the gain in computational efficiency is not only due to the reduction in grid size but also due to a decrease of the cell aspect ratio near the wall, which reduces computational stiffness.

Figure 4.2: Law of the wall<sup>4</sup>

In order to make a choice, the  $y^+$  values obtained from the available meshes (see Chapter 6 on the grid convergence study) were looked at. The conclusion is that in order to meet the constraint of  $y^+ \leq 1$ , an even finer mesh will need to be created. This means that a new computational grid will easily exceed 7 million cells, which is very time consuming to handle. Keep in mind that the realistic lung geometry is complex; this means that it is very difficult to properly capture the viscous layer everywhere.

Considering the previous, the choice is made to use adaptable wall functions (for more information about adaptable wall functions, see Section 5.2.3).

<sup>4</sup> This data was obtained for a fully developed flow in a smooth cylindrical pipe

## 5. Simulation model

The next step is to import the computational domain into the RANS solver of the Fine/Hexa software (Numeca, Brussels, Belgium). RANS is the obvious choice, for LES is too time consuming (see Section 2.2 of the literature study).

Now looking at the flow physics, first a choice has to be made between solving for laminar or turbulent flow. Laminar flow is characterized by smooth, constant fluid motion and occurs at low Reynolds numbers. Here viscous forces are dominant. Turbulence, however, is dominated by inertial forces, which tend to produce flow instabilities such as chaotic eddies and vortices and occurs above a critical Reynolds number that depends on the specific case. As a relative example, for flow in a pipe of diameter  $D$ , experimental results show that for a fully developed flow, laminar flow occurs when  $Re_D < 2300$  and turbulent flow occurs when  $Re_D > 4000$ . Between these two extremes lies the transitional regime, where both flow regimes are possible depending on other factors such as pipe roughness and flow uniformity. In this thesis the inlet Reynolds number,  $Re_D$  varies from 600 to 1200 and 2400 for respectively inhalation rates of 15, 30 and 60 l/min. This is at the inlet where the flow is more or less laminar, but going further downstream turbulence is noticed to occur after the laryngeal jet, where the local velocity strongly increases and so does the local Reynolds number. De Geeter (De Geeter, 2010) also found this when he performed both laminar and turbulent simulations with the Fluent software (Ansys, Canonsburg, PA) on the realistic from CT scan data derived geometry.

Considering this, the SST  $k-\omega$  model turbulence model is chosen because its ability to predict transitional flow phenomenon.

This chapter then describes the complete simulation model, ranging from the governing equations to the solver settings and boundary conditions used along the geometry.

### 5.1. Fluid model

For the fluid model the air is considered to be Newtonian, homogenous and incompressible. Consequently for the whole flow domain a constant density of  $1.2 \text{ kg/m}^3$  is taken.

### 5.2. Numerical Method

#### 5.2.1. Reynolds Averaged Navier-Stokes equations

The general Navier-Stokes equation (without source term) in a Cartesian frame of reference integrated over a control volume  $V$  is given by:

$$\frac{\partial}{\partial t} \iiint_{\Omega} U \, d\Omega + \iint_S \vec{F} \cdot d\vec{S} = \iint_S \vec{G} \cdot d\vec{S} \quad (5.1)$$

where

$$U = (\rho, \rho u, \rho v, \rho w, \rho E)^T$$

With  $U$  being the set of conservative variables and  $\vec{F}$  and  $\vec{G}$  are respectively the inviscid and viscous fluxes. From these general equations, the equations for conservation of mass and momentum for an incompressible steady on-average flow, which are relevant to this thesis, can be derived.

The Reynolds averaged equations are then obtained by averaging the conservation laws over a time interval  $T$ , large enough with respect to the time scales of the turbulent fluctuations, but small enough with respect to all other time-dependent effects. Time averaging is appropriate for stationary

turbulence. Consider now an instantaneous flow variable expressed by  $f(x, t)$ . Its time average,  $F_T(x)$  is then given by:

$$F_T(x) = \lim_{T \rightarrow \infty} \frac{1}{T} \int_t^{t+T} f(x, t) dt \quad (5.2)$$

Furthermore, for a stationary turbulent flow, the instantaneous velocity  $u_i(x, t)$  can also be expressed as the sum of a mean,  $\bar{u}_i(x)$  and a fluctuating part,  $u'_i(x, t)$  such that:

$$u_i(x, t) = \bar{u}_i(x) + u'_i(x, t) \quad (5.3)$$

Thus after Reynolds averaging and some rewriting the Reynolds-Averaged Navier-Stokes equation (RANS) is obtained, as depicted in equation (5.4). Here  $\tau_{ij}^R = -\rho \bar{u}'_i \bar{u}'_j$  is known as the important Reynolds-stress tensor, which couples the mean flow to the turbulence.

$$\rho \frac{\partial u_i}{\partial t} + \rho \bar{u}_j \frac{\partial \bar{u}_i}{\partial x_j} = -\frac{\partial \bar{p}}{\partial x_i} + \frac{\partial}{\partial x_j} (\bar{\tau}_{ij} + \tau_{ij}^R) \quad (5.4)$$

Now six unknown quantities are produced but no extra equations are created. In order to close the system we will need to introduce some additional equations. This is generally referred to as the closure problem.

### 5.2.2. Turbulence model

As already suggested in Section 2.2 of the literature study, the M-SST  $k-\omega$  turbulence model is selected within the Fine/Hexa solver (Numeca, Brussels, Belgium). Menter (1994) proposed this blended two equation model. It combines the advantages of the Wilcox  $k-\omega$  model and the standard  $k-\varepsilon$  model and has a higher accuracy in predicting flow separation.

The  $k-\omega$  model is used in the inner parts of the boundary layer, ranging from the viscous sub-layer down to the solid wall. In the free-stream, however, the SST formulation switches to the  $k-\varepsilon$  model, in a  $k-\omega$  formulation, and thereby avoids the common  $k-\omega$  problem of being too sensitive to the inlet free-stream turbulence properties.

By definition, two equation models include two extra transport equations to represent the turbulent properties of the flow. The basis for all two equation models is the Boussinesq eddy viscosity Hypothesis as given in equation (5.5), which relates the Reynolds stress tensor to the mean velocity gradients. So in order to solve the previous system of equation (5.4), the Reynolds stress tensor is modeled using the following assumption:

$$\rho \bar{u}'_j \bar{u}'_i = \mu_t \left( \frac{\partial \bar{u}_i}{\partial x_j} + \frac{\partial \bar{u}_j}{\partial x_i} \right) - \frac{2}{3} \left( \rho k + \mu_t \frac{\partial \bar{u}_k}{\partial x_k} \right) \delta_{ij} \quad (5.5)$$

Here  $\mu_t$  is the turbulent eddy-viscosity and  $k$  is the turbulent kinetic energy.

The turbulent kinetic energy and the specific dissipation rate can now be obtained from the following two transport equations, as defined by Menter (Menter, 1994):

$$\frac{\partial k}{\partial t} + \bar{u}_j \frac{\partial k}{\partial x_j} = P_k - \beta^* k \omega + \frac{\partial}{\partial x_j} \left[ \left( \nu + \frac{\nu_t}{\sigma_k} \right) \frac{\partial k}{\partial x_j} \right] \quad (5.6)$$

$$\frac{\partial \omega}{\partial t} + \bar{u}_j \frac{\partial \omega}{\partial x_j} = \frac{\gamma}{\nu_t} P_k - \beta \omega^2 + \frac{\partial}{\partial x_j} \left[ \left( \nu + \frac{\nu_t}{\sigma_\omega} \right) \frac{\partial \omega}{\partial x_j} \right] + 2(1 - F_1) \sigma_{\omega^2} \frac{1}{\omega} \frac{\partial k}{\partial x_j} \frac{\partial \omega}{\partial x_j} \quad (5.7)$$

With  $\sigma_k$  and  $\sigma_\omega$  being the turbulent Prandtl numbers for  $k$  and  $\omega$  respectively and  $\nu_t$  the turbulent viscosity. For a detailed description of all constants and variables the reader is referred to the paper of Menter (1994) and the Fine/Hexa user manual.

At the wall boundary,  $k = 0$  and the specific dissipation rate,  $\omega$  asymptotically tends to infinity as  $\sim 1/y^2$ . It was then suggested to use the following boundary condition:

$$\omega = \frac{60\nu}{\beta d^2} \quad (5.8)$$

Here  $d$  is the distance from the wall to the first cell center closest to the wall.

### 5.2.3. Wall functions

Wall functions are used to mimic the presence of the non-linear variations of the flow properties throughout the turbulent boundary layer. They define the shear stress at the cell faces laying on the solid boundary, as well as the values of  $k$  in the vicinity of the wall. The earliest ‘standard’ wall functions required the grid point closest to the wall to lie in the logarithmic layer. This constraint is too strict and is often violated by the grid. Furthermore, if the first grid point lies in the viscous layer, standard wall functions are generally reported very inaccurate.

In response to this, wall functions that do not have this restriction are called adaptive wall functions. Consequently the first grid point closest to the wall can lie in the viscous layer ( $y^+ < 5$ ) or in the logarithmic layer. Only the buffer layer presents a challenge to the adaptive approach.

In order to obtain values for  $k$  in the first cell closest to the wall, adaptable wall functions are used which were derived from Direct Numerical Solution (DNS) data (see Hakimi et al. (Hakimi, 1997) and the Fine/Hexa user manual for more details). The wall functions for  $k$  are then curve fitted with polynomials to the DNS data.

To attain values for  $\omega$  is more of a numerical challenge due to its infinite value at the wall. The procedure to extract these values is described in the paper of Kalitzin et al. (Kalitzin, et al., 2005), i.e. we first consider the general transport as given by eq. (5.7), which reduces to the following form in the viscous layer:

$$-\beta(\omega^+)^2 + \frac{\partial^2 \omega^+}{(\partial y^+)^2} = 0 \quad (5.9)$$

Here  $\omega^+ = \frac{\omega\nu}{u_t^2}$ , is the non dimensional form of  $\omega$ . The solution of the latter equation for smooth walls is given by eq. (5.10):

$$\omega^+ = \frac{6}{\beta(y^+)^2} \quad (5.10)$$

For the logarithmic layer, after some deriving the expression for the specific dissipation rate becomes:

$$\omega^+ = \frac{1}{\kappa\sqrt{\beta^*}y^+} \quad (5.11)$$

In the intermediate region,  $\omega^+$  is approximated by an interpolation between the values of the viscous and logarithmic layer:

$$\omega^+ = \sqrt{(\omega_{viscous}^+)^2 + (\omega_{logarithmic}^+)^2} \quad (5.12)$$

### 5.2.4. Solver settings

After defining the boundary conditions, relevant and working solver settings have to be provided. This is not always straightforward since some of them, mostly parameters related to the preconditioning, lead to a diverging solution. The computer software used, FINE™/Hexa has a user environment integrated solver, which is a multipurpose unstructured code for 2D and 3D flows in complex geometries using the latest numerical developments in CFD (Numeca, Brussels, Belgium).

#### 5.2.4.1. Preconditioning

Fine/Hexa solves the coupled compressible RANS equations. This means that the governing equations are solved simultaneously as a set, or vector, of equations. Here caution has to be maintained, since the applications described in this thesis are of incompressible nature. Commonly in the low subsonic Mach number regime, time marching algorithms designed for compressible flow converge very slowly.

This problem is however overcome by making a small modification to the governing system of equations, called preconditioning. Preconditioning is derived from the artificial compressibility method introduced for incompressible flows by Chorin (1967).

The idea of preconditioning is to multiply the time derivatives of the dependant variables with a matrix,  $\Gamma^{-1}$ . This can be done, because for steady state applications solved by time marching algorithms, the time derivatives of the unknowns in the flow equations are of no physical meaning and can therefore be modified without altering the final steady state solution. The main property of this preconditioning matrix is that it removes the stiffness of the eigenvalues.

The general form of the preconditioned Reynolds-Averaged Navier-Stokes equations excluding source terms and including turbulence, written in a Cartesian from of reference and integrated over a control volume  $\Omega$ , is expressed as:

$$\iiint_{\Omega} \Gamma^{-1} \frac{\partial Q}{\partial t} d\Omega + \iint_S \vec{F} \cdot d\vec{S} = \iint_S \vec{G} \cdot d\vec{S} \quad (5.13)$$

with

$$Q = (p_g, u, v, w, E_g, \rho k, \rho \varepsilon)^T$$

$\vec{F}$  and  $\vec{G}$  are respectively the inviscid and viscous fluxes, the variable  $p_g = p - p_{ref}$  is the gauge pressure and  $E_g$  is the total gauge energy.

Furthermore, the general form of the preconditioning matrix,  $\Gamma^{-1}$  for both compressible and incompressible fluids is a combination of those suggested by Turkel (Turkel, 1987) and Choi and Merkle (Choi, et al., 1985) and is given by:

$$\Gamma^{-1} = \begin{bmatrix} \frac{1}{\beta^2} & 0 & 0 & 0 & 0 & 0 & 0 & \cdots & 0 \\ \frac{(1+\alpha)u}{\beta^2} & \rho & 0 & 0 & 0 & 0 & 0 & \cdots & 0 \\ \frac{(1+\alpha)v}{\beta^2} & 0 & \rho & 0 & 0 & 0 & 0 & \cdots & 0 \\ \frac{(1+\alpha)w}{\beta^2} & 0 & 0 & \rho & 0 & 0 & 0 & \cdots & 0 \\ \frac{\alpha \vec{v}^2 + E_g}{\beta^2} (-1)^* & 0 & 0 & 0 & \rho & 0 & 0 & \cdots & 0 \\ 0 & 0 & 0 & 0 & 0 & 1 & 0 & 0 & \cdots & 0 \\ 0 & 0 & 0 & 0 & 0 & 0 & 1 & 0 & \cdots & 0 \end{bmatrix} \quad (5.14)$$

(\*the term -1 should be added in compressible cases only)

In order to have a proper preconditioning, there are four user defined parameters that need to be set and tuned:  $T_{ref}$ ,  $p_{ref}$ ,  $\alpha$  and  $\beta$ . The first two parameters,  $T_{ref}$  and  $p_{ref}$  were taken equal to the reference temperature and pressure defined by the fluid, air in this case. The parameter  $\alpha$  is set to be -1, as this is far the best value found considering the convergence rates of several computations accomplished with the central scheme. This optimal value adds an additional amount of artificial dissipation. Furthermore, the  $\beta$  parameter is imposed by the user through a coefficient  $\beta^*$  and a characteristic velocity  $U_{ref}$ , here taken as the inlet velocity:

$$\beta^2 = \beta^* \max(U_{ref}^2, U_{loc}^2) \quad (5.15)$$

with  $U_{loc}$  being the local velocity. The parameter  $\beta^*$  should normally increase as the Reynolds number decreases and may vary across several orders of magnitude. Also, one has to keep in mind that a too large value of  $\beta^*$  will introduce excessive artificial dissipation into the solution.

#### 5.2.4.2. Methods

As already stated before, computations are performed using the RANS equations with the M-SST k- $\omega$  turbulence model. For the spatial discretisation use is made of a second order central finite volume scheme with Jameson type dissipation of second and fourth order (Jameson, et al., 1981). Considering the time discretisation, an explicit fourth order Runge-Kutta scheme is used to march the solution in time towards steady state.

A Multigrid V-cycle strategy containing 4 grid levels is used for accelerating convergence of the solution (Hirsch, et al., 1991). The power of this method lies in the fact that it damps most of the low frequency errors that cannot be damped by explicit schemes. For stability reasons the Courant-Friedrichs-Lowy (CFL) number is kept constant at a value of 3. The flow is assumed to be converged when the dimensionless mass and momentum residuals were less than  $10^{-3}$ . (For a more detailed description on the different numerical schemes and settings, the reader is referred the relevant papers and to the Fine/Hexa user manual)

### 5.3. Boundary conditions

#### 5.3.1. Inlet

At the inlet successively a mass flow of 15, 30 and 60 liter/min is applied for inspiration. The different rates correspond respectively to breathing during a light activity (resting), normal activity and heavy activity (exercising). These boundary conditions are specified at the inlet in the form of the different velocity components together with the static pressure and are applied as a uniform profile. According to Heenan et al. (2003), different inlet profiles do not have any influence on the results. Furthermore, when solving the RANS-equations combined with a two-equation turbulence model for subsonic flow also an estimate for the turbulent kinetic energy and turbulent specific dissipation rate has to be given. A well known formula for the estimation of the turbulent kinetic energy is given by:

$$k_{inlet} = \frac{3}{2} (I_{inlet} u_{inlet})^2 \quad (5.16)$$

Where  $u_{inlet}$  is the mean inlet velocity and  $I_{inlet}$  is the inlet turbulent intensity usually taken as 5% for internal flows. For this case, as air is inspired from still atmosphere, the turbulence intensity levels will generally be very small. Brouns et al. (2007) performed simulations with a turbulence intensity of 5% and 10% and concluded that this variation has no influence on the turbulent kinetic energy in the pharynx and trachea. Also Heenan et al. (2003) noticed that these turbulence parameters have little influence on the results. The turbulent dissipation rate can then be estimated by:

$$\epsilon_{inlet} = \frac{c_\mu^{3/4} k_{inlet}^{3/2}}{l} \quad (5.17)$$

Consequently the turbulent specific dissipation rate is given by:

$$\omega_{inlet} = \frac{\epsilon_{inlet}}{k_{inlet}} \quad (5.18)$$

In eq. (5.17),  $c_\mu$  is a constant taken equal to 0.09 for most models and  $l$  is the turbulent length scale estimated by:

$$l = 0.1 D_h \quad (5.19)$$

with

$$D_h = \frac{4A}{P} \quad (5.20)$$

where  $D_h$  is the hydraulic diameter,  $P$  the perimeter and  $A$  the area of the inlet section.

#### 5.3.2. Outlet

From the CT scan at two different lung levels it is possible to extract the mass fractions at each lung lobe, which can be used as boundary conditions. These boundary conditions are fixed per lobe and do not provide us with any information on the mass outflow at each outlet. Because the kind of boundary conditions is crucial for the simulation, a choice has to be made between two options: Using mass outflow or pressure outlet boundary conditions.

De Geeter (2010) made the assessment between these different boundary conditions and first considered the choice of using mass outflow conditions. The first problem encountered consists of obtaining the outflow condition at each of the actual outlets. For this the mass fraction at a certain

lung lobe is taken and divided by the number of outlets to obtain an outflow condition at each outlet. However, when using this approach, and thus using the same mass outflow at each outlet of a certain lobe, at some locations a relatively large mass flow is then forced through a smaller outlet, which results in unrealistic pressure drops (see Figure 5.1) This problem is highly unwanted and is also reported for example by Luo et al. (Luo, et al., 2008), which made them switch to pressure outlets.

An attempt was then made to resolve this trouble by using a weighted average over the outlet area. This approach actually solved the problem at some outlets, but also worsened the situation at other locations.

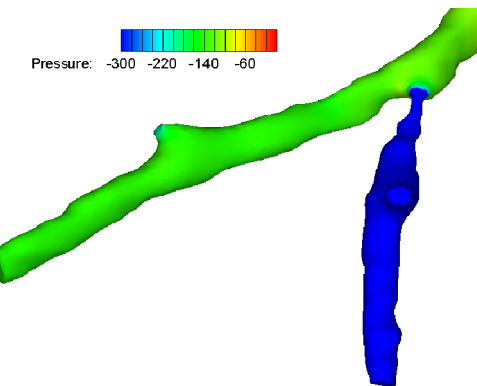


Figure 5.1: Unrealistic pressure drop in an outlet<sup>5</sup>

For this reason De Geeter (2010) switched to using pressure outlets. This change solves all the previous instability problems and is actually also a more realistic boundary condition as the flow is driven by pressure. As a consequence the small outlets acquire less mass flow, as it should be. Therefore this approach is chosen for the current study as well. The drawback, however, is that it takes some time to obtain the required pressures at each lung lobe.

In order to acquire pressure outlet boundary conditions, first the pressure at each lung lobe is set uniformly. Then the pressures are iteratively changed to match the given mass fractions at each lobe, as suggested by De Backer et al. (2008). This was done starting from the average pressure at the outlets of each lobe, computed using the previous case with the mass outflow boundary conditions. The erroneous pressures were then first removed from the average. This gave a first indication. Next the pressure is altered in order to match the mass fraction boundary condition at each lobe. For example at lung lobes where the mass fraction is too high, the pressure needs to be increased and vice versa. This is done until the obtained mass fraction percentage is acceptable.

### 5.3.3. Wall

The walls are assumed to be adiabatic and have the no-slip condition.

<sup>5</sup> Figure taken from the paper of De Geeter et al. (2010)

## 6. Grid convergence Study

### 6.1. Introduction

In this chapter a grid independence study is performed for the realistic CT-scan derived lung geometry. This was done in order to have a mesh independent solution for the given complex geometry. All meshes are unstructured hybrid meshes and were created using the commercially available software Hexpress Hybrid (Numeca, Brussels, Belgium). The mesh consists largely out of hexahedral elements, for example in the boundary layer, and prism elements (see Figure 4.1), but also some tetrahedral elements. The procedure for the grid independence study as followed is given in the paper of Longest et al. (Longest, et al., 2007).

### 6.2. Results

The grid convergence study is performed using a coarse (910,000 cells), a medium (2,320,000 cells) and two fine meshes (5,230,000 cells and 6,820,000 cells), depicted respectively as 3, 2, 1 and 0 in Table 6.1. Note that the finest mesh of 6,820,000 cells is created to check whether the solution still changes compared to the 5,230,000 cells mesh.

First, grid convergence is evaluated using a relative error measure of normalized velocity magnitude at a normal breathing rate between, in this case, the 5.23 million cells (depicted as 1) and the 2.32 million cells (depicted as 2) mesh:

$$\varepsilon_{21,i} = \left| \frac{V_{i,2} - V_{i,1}}{V_{i,1}} \right| \quad (6.1)$$

Consequently the solution at 1000 consistent points is extracted at three important flow regions in the geometry, namely the trachea and the first left and right bifurcation (see Figure 3.2). At the trachea the solution is extracted at the central saggital plane along the line of A1-A2, as depicted in Figure 6.1. For the first left and right bifurcation the solution is extracted at the middle of the cutting plane. In order to provide an initial scalar measure of grid convergence also the RMS value of the relative error is computed:

$$\varepsilon_{21,rms} = \left( \frac{\sum_{i=1}^{10^3} \varepsilon_i^2}{10^3} \right)^{\frac{1}{2}} \quad (6.2)$$

In theory, grid convergence measures should be based on refining the grid by a factor of 2 (grid halving). However, this means that the total amount of cells in the mesh would increase by a factor of 8 for three dimensions and thus is not attainable in this case. In this way, relative error values must be adjusted to account for cases in which grid halving is not applied, i.e. when  $r < 2$ . To extrapolate  $\varepsilon_{rms}$  values to conditions consistent with grid halving, the grid convergence index (GCI) has been suggested by Roache (Roache, 1992). The GCI, which is a measure of the percentage the computed value is away from the value of the asymptotic numerical value, is given by eq. (6.3), as taken from the paper of Longest et al. (Longest, et al., 2007):

$$GCI_{21} = F_s \frac{\varepsilon_{21,rms}}{r^p - 1} \quad (6.3)$$

Where  $F_s$  is a safety factor advised to be taken as 1.25 for comparing three meshes,  $p$  is the order of convergence and should be equal to 2 based on using a second order space discretization method. Furthermore, the grid refinement factor,  $r$  is recommended to have a greater value then 1.3 (Longest, et al., 2007). The definition to calculate  $r$  is, as given by eq. (6.4):

$$r_{21} = \left( \frac{N_1}{N_2} \right)^{\frac{1}{3}} \quad (6.4)$$

With  $N$  being the grid size and  $D$ , the dimension here taken equal to 3. As can be seen in Table 6.1 the values for  $r$  just meet the requirement of being larger than 1.3. Note that with the complex geometry it is not straightforward to obtain a higher value for  $r$  as this implies a large increase in mesh size.

Name	Symbol	Value
Grid size	$N_0, N_1, N_2, N_3$	6,82, 5.23, 2.32, 0.91 ( $\times 10^6$ ) cells
Grid refinement	$r_{20}$	1.43
	$r_{21}$	1.31
	$r_{32}$	1.37

Table 6.1: Grid size and refinement factors with (0) depicting the 6.82 million, (1) the 5.23 million, (2) the 2.32 million and (3) the 0.91 million mesh

The results of the grid convergence study for the 4 meshes at three different sections in the mesh are then given in Table 6.2, 6.3 and 6.4. Moreover, Figure 6.2 shows the velocity magnitude at the three sections for the four different mesh sizes.

Grid size ( $\times 10^6$ )	$\epsilon_{rms}$ (%)	GCI (%)
<b>0.91 - 2.32</b>	31.89	45.45
<b>2.32 - 5.23</b>	13.37	23.34
<b>2.32 - 6.82</b>	18.17	21.73

Table 6.2: RMS error and GCI for the normalized velocity magnitude profile extracted at the trachea section

Grid size ( $\times 10^6$ )	$\epsilon_{rms}$ (%)	GCI (%)
<b>0.91 - 2.32</b>	21.0	29.94
<b>2.32 - 5.23</b>	3.75	6.55
<b>2.32 - 6.82</b>	4.93	5.89

Table 6.3: RMS error and GCI for the normalized velocity magnitude profile extracted at the first left bifurcation section

Grid size ( $\times 10^6$ )	$\epsilon_{rms}$ (%)	GCI (%)
<b>0.91 - 2.32</b>	11.90	16.96
<b>2.32 - 5.23</b>	6.23	10.87
<b>2.32 - 6.82</b>	8.26	9.88

Table 6.4: RMS error and GCI for the normalized velocity magnitude profile extracted at the first right bifurcation section

When having a first look at the results and in particular at the RMS values, it seems that the solution between the coarse and medium mesh is still subject to some change. We can conclude that the mesh of 910,000 cells is indeed still too coarse. Also, especially in the trachea section, the solution of the 2,320,000 cells mesh still changes with a measure of 13.37% with respect to the 5,230,000 cells and 18.17% with respect to the finest mesh, as shown in Table 6.2. Therefore, the medium mesh is also considered still too ‘coarse’. It is noticed that the trachea section is most critical since the

deviation between the velocity profiles of the different meshes is the largest here. This is because of the flow separation which is seen to occur after the glottis region.

Furthermore, the GCI values are seen to decrease with the successive grid refinements on all three sections.

Let us consider now whether the solution between the two finest meshes with grid size  $N_0$  and  $N_1$  still changes. The RMS error between both meshes as compared with the medium mesh is calculated and depicted in Table 6.5. As can be seen, the solution of the finest mesh is not subject to much change anymore compared to the fine mesh. Moreover, the maximum difference in normalized velocity magnitude does not exceed 5% in the critical trachea section. Hence the 5,230,000 cells mesh suffices for accurate flow simulations.

Section	$\epsilon_{rms}$ (%)
Trachea	4.8
First Left Bifurcation	1.18
First Right Bifurcation	2.03

Table 6.5: RMS error between the 6.82 million and the 5.23 million mesh at three sections in the geometry

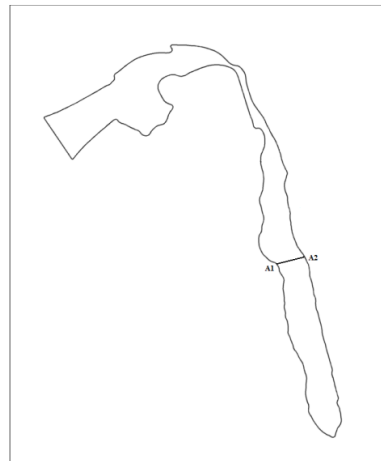


Figure 6.1: location of the velocity profile as extracted from A1 to A2 at the central saggital plane

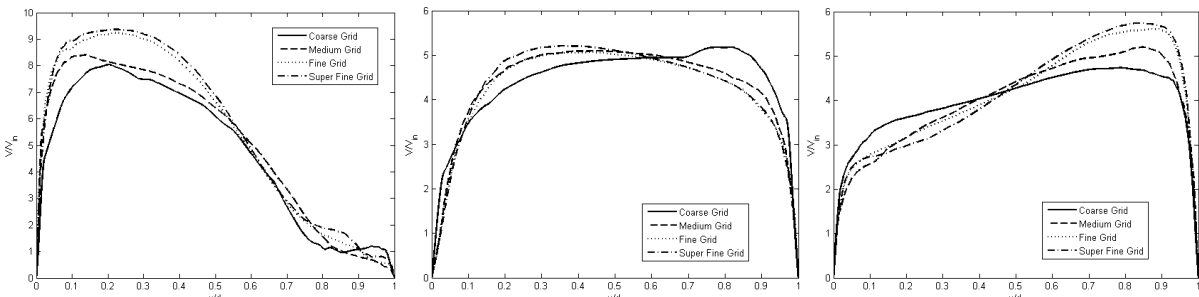


Figure 6.2: Normalized velocity magnitude results for the different mesh sizes (left) at the trachea, (middle) at the first left bifurcation and (right) at the first right bifurcation

### 6.3. Conclusion

Regarding the results of Table 6.5, one can say that with an even finer mesh of 6,820,000 cells the solution changes only with a maximum of 4.8% with respect to the 5.23 million. In conclusion, for all calculations performed in the next chapters the fine mesh of 5,230,000 cells is considered.

## 7. Results application I: The simplified geometry

In this section the results obtained for the simplified mouth-throat geometry are given. This chapter will be brief however, because the main work of this thesis is with respect to the realistic lung geometry. Simulations are performed in the first place to test and validate the Fine/Hexa solver and also to give an assessment between flow phenomenon in the simplified and realistic geometry (which are depicted in Chapter 8). Note that simulations with the simplified geometry have already been performed in the past with a different solver, however. Consequently a comparison will be made with results obtained with the other solver and with experiments from the literature. Observe that in the previous chapters, the simulation and mesh features are discussed for the realistic geometry. As for the simplified model, they are mostly the same with a few exceptions which will be discussed in section 7.1 (Numerical Methods). In section 7.2 and 7.4 the geometry and the mesh are presented respectively. In section 7.3 the experimental set-up will be briefly presented. The last section deals with the results and experimental validation of the simulations. Here relevant to the experiment, the results for the velocity magnitude and turbulent kinetic energy are given and discussed.

### 7.1. Numerical Methods

For the overall simulation model the reader is referred to Chapter 5. There are, however, a few deviations from this model, since it depicts the realistic model.

First, with respect to the experimental results, the flow equations are solved for the simplified model at a normal breathing rate of 30 l/min and also 15 l/min. As for the outlet a corresponding outflow condition is imposed, since the pressure at the outlet is unknown. Moreover, due to the simplified nature of the geometry it was possible to create a sufficiently fine mesh in the boundary layer. In this way the  $y^+$  of the first cell closest to the wall was kept about 1. Therefore the low Reynolds  $k-\omega$  SST turbulence model was considered suitable for solving the equations.

### 7.2. Geometry of the model

In Figure 7.1 the geometry of the simplified model as created by Brouns et al. (2007) is shown. Moreover, from Figure 2.7 in the literature chapter, it can be seen how this smoothed symmetric geometry is derived from a realistic lung geometry with the use of preliminary CFD simulations. Most physical features like the shape of the mouth cavity, position of the trachea and the epiglottis are maintained in the simplified model. In this way critical flow features like the shape and location of the tracheal jet, the location of the maximum velocity and recirculation zones are preserved.

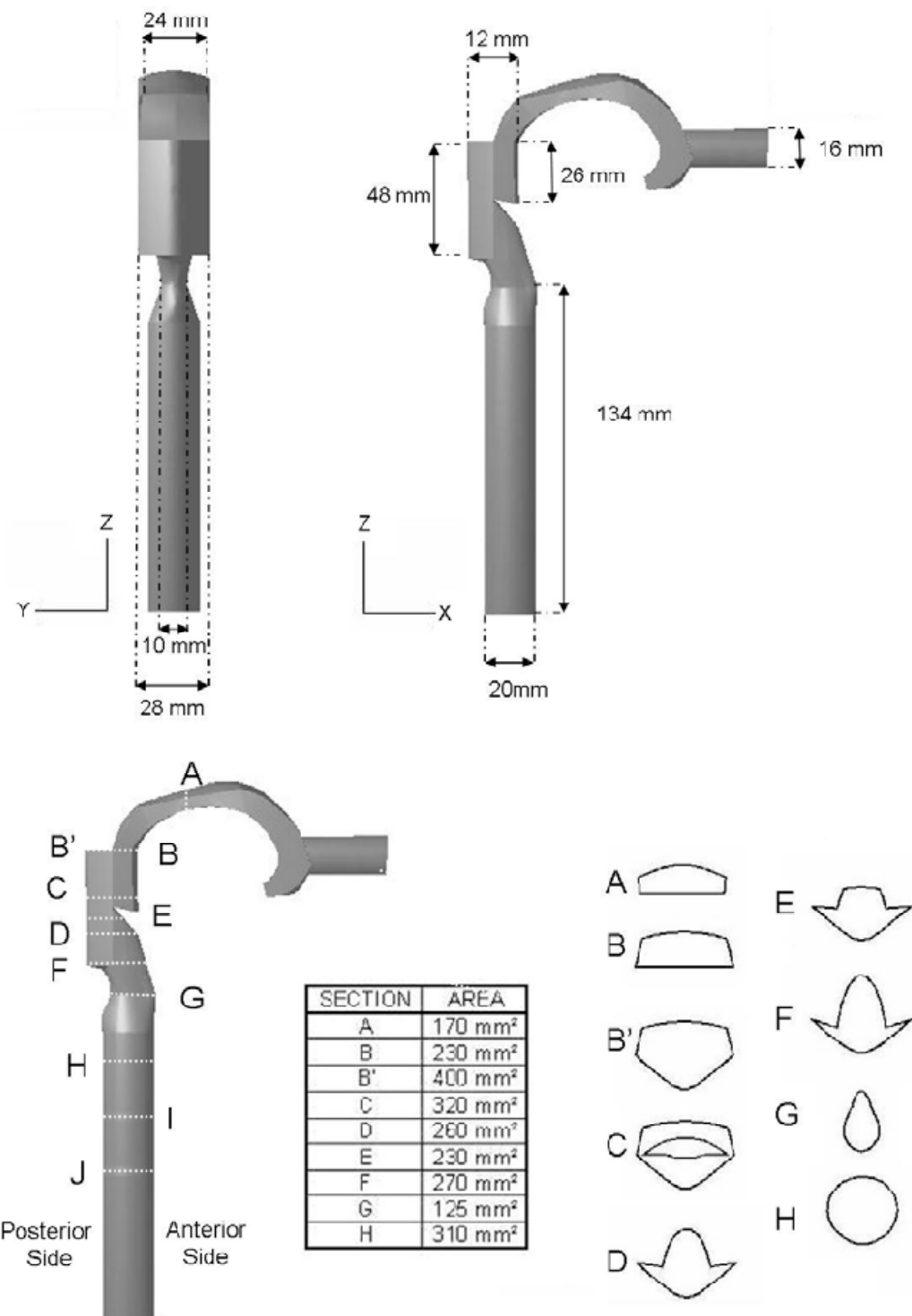


Figure 7.1: Geometry of the simplified model

### 7.3. Experimental set-up

The experiment was performed by Brouns et al. (2007) and was done with the use of PIV. In this way a one-block transparent physical model is made from the computer designed model using stereolithography. A water-glycerin mixture, with a viscosity of  $5.88 \times 10^{-6} m^2/s$  as determined with the AVS300 viscosimeter (from Schott Gerate) at 25.2°C, was pumped in a reservoir placed about 1.5 meter above the model to ensure a fully developed profile. Dynamic similarity was achieved by

matching the Reynolds number. Furthermore, the reservoir has an inlet which is connected to a pump, an outlet connecting the model and an overflow exit which provides a constant reservoir level. A New Wave Minilasell Nd-Yag laser (532 nm wavelength, 100mJ/pulse) was used and synchronized with a pulse separation, which depends on the flow rate. For the tracer particles 10  $\mu\text{m}$  hollow glass spheres were taken, which shift 5 pixels between an image pair depending on the pulse separation. 4000 image pairs were recorded approximately for the case of 30 l/min and 2000 image pairs for the case of 15 l/min. The vector fields were generated using cross-correlation fast Fourier transforms and the final interrogation region consists of 32×32 pixels with an overlap of 50%. For a more detailed description of the experimental set-up and model creation, the reader is referred to the paper of Brouns et al. (2007).

## 7.4. Mesh

An unstructured hexahedral mesh of about 800,000 cells with a sufficient number of grid points in the boundary layer is used for the simulation. Due to the somewhat complex structure of the airway model, an unstructured mesh was chosen in order to create a high quality mesh.

## 7.5. Results

In this section the acquired results with RANS are compared with PIV experiments and results obtained with a different solver. These results were obtained by Brouns et al. (2007) and Jayaraju et al. (2007) at various model cross-sections (see left part of Figure 7.5). Note that from the experimental results, only the two-component velocity magnitude and 2 component kinetic-energy profiles could be extracted. However, since the kinetic energy equation in RANS implicitly includes all 3 components, a direct comparison with the experimentally measured 2 component kinetic energy is not possible. Therefore the focus in this chapter will be on the comparison between the 2 component velocity magnitudes.

### 7.5.1. Velocity and turbulent kinetic energy

The left part of Figure 7.2 and Figure 7.3 shows the simulated velocity magnitude for the breathing rates of 15 and 30 l/min, whereas the right part shows the kinetic energy for the different breathing rates for the simulation. In order to portray these results in a proper way, a cutting plane is made at the central sagittal plane, splitting the model exactly in the middle.

The air enters through the mouthpiece into the mouth-cavity and takes from here a bend around the tongue. Just before the bend some of the air is drawn into a recirculation zone. The flow then accelerates in the middle part of the mouth due to a decrease in cross-sectional area. Further down, the flow expands in the pharynx region due to an increase in area. Now the flow velocity is first reduced, but again accelerates due to a reduction in cross-sectional area. At the end of the pharynx the flow is guided towards the anterior side of the trachea and expands again in the larynx region in the form of a jet, the laryngeal jet. Here the peak velocity occurs, about 2.8 m/s for the case of 15 l/min and 5.8 m/s for the case of 30 l/min. Furthermore, from the right part of Figure 7.2 and Figure 7.3 it can be seen that turbulence only really occurs after the glottis region for both breathing rates. Comparing the results for 15 and 30 l/min, one does not notice much difference. It can be seen though that the laryngeal jet is less pronounced and shorter for 30 l/min.

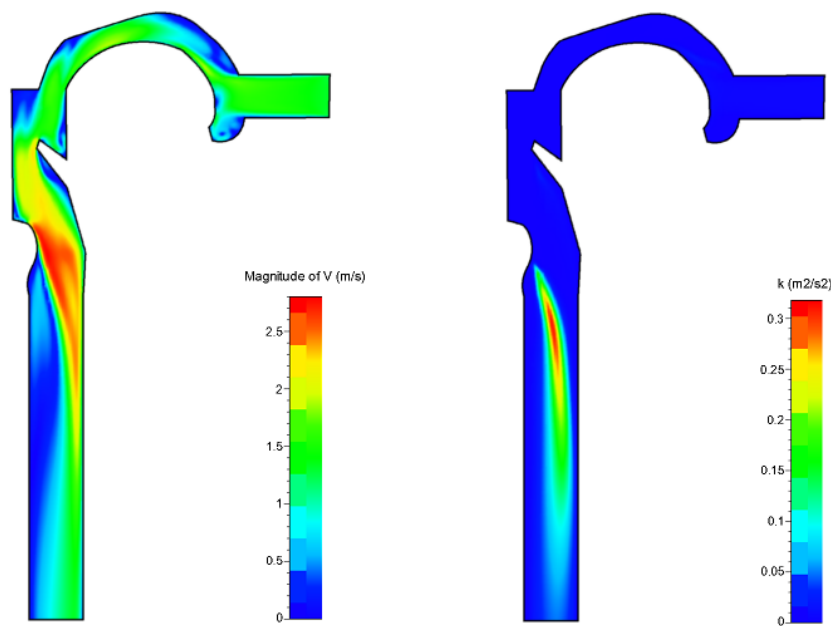


**Figure 7.2:** Results (left) of the simulation for the velocity magnitude and (right) for the turbulent kinetic energy performed at an inlet mass flow of 15 l/min

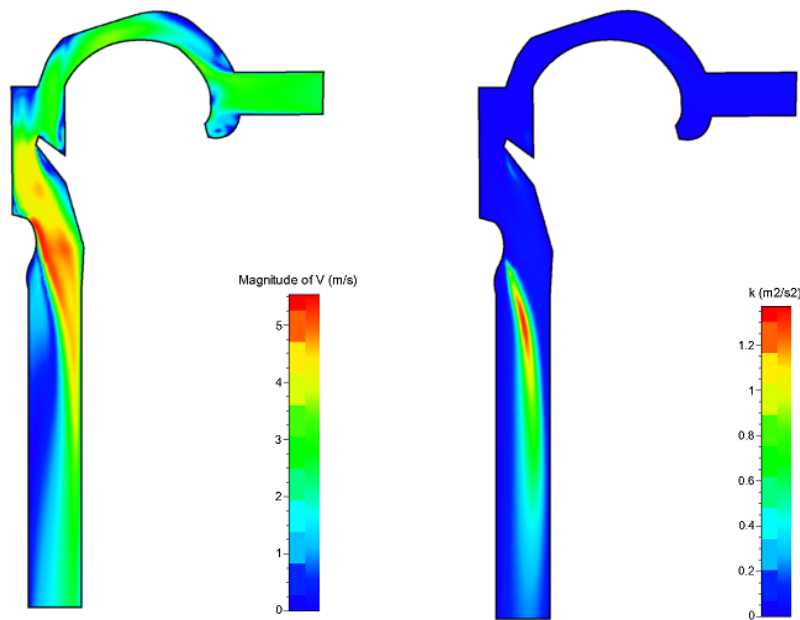


**Figure 7.3:** Results (left) of the simulation for the velocity magnitude and (right) for the turbulent kinetic energy performed at an inlet mass flow of 30 l/min

### 7.5.2. Experimental validation

In Figure 7.4 both the experimental and the computational result for the normalized 2 component velocity magnitude ( $u_x$  and  $u_z$ ) are shown. The experiment was performed at a breading rate of 30 l/min. Given the inlet diameter, this corresponds to a flow Reynolds number,  $Re_D$  of about 2500 which finds itself in the transitional regime.

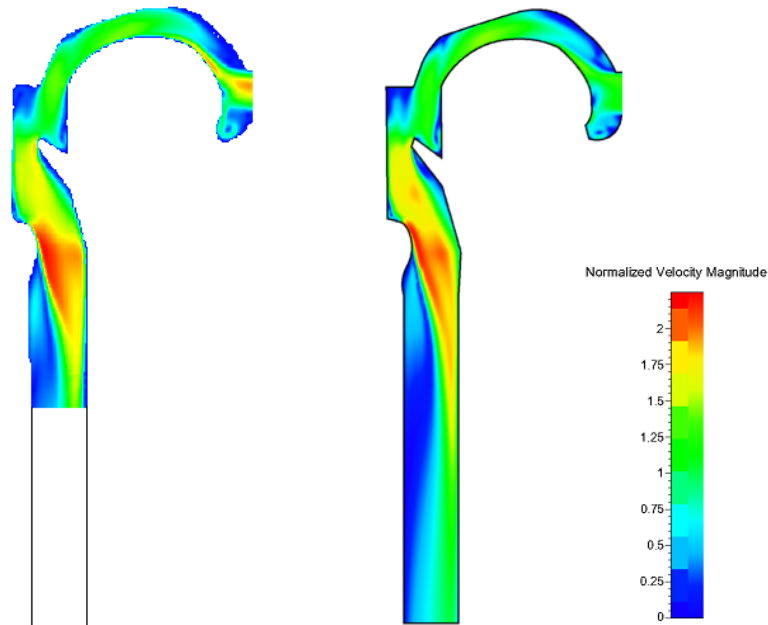


Figure 7.4: Results obtained for 30 l/min, (left) from the experiment<sup>6</sup> and (right) obtained from RANS simulation with Fine/Hexa

In order to compare in a more quantitative manner, velocity profiles are extracted at four cross-sections in the geometry (see left part of Figure 7.5). Also given in the right part of this figure are the corresponding streamlines. Here one also notices the two recirculation zones. Figure 7.6 shows a comparison with the experimental results and the RANS results obtained on the same mesh with the Fluent software (Ansys) for the normalized 2 component ( $u_x$  and  $u_z$ ) velocity magnitude. The velocity profiles were extracted from the posterior to the anterior side (from left to right). As can be seen in Figure 7.6 the results of Fine/Hexa and Fluent, even less accurately than Fine/Hexa, over predict the velocity peaks at the anterior side of the geometry in comparison with the PIV measurements. As for the velocity peaks at the posterior side, they are slightly better predicted with the Fine/Hexa solver. In the paper of Jajayru et al. (2007) also LES results are shown, which offer a much better approximation of the experimental results.

### 7.5.3. Conclusion

The results obtained with RANS have been seen to reasonably reproduce the experimental results and predict the distinct flow phenomena in the simplified geometry in comparison with Fluent. Hence the Fine/Hexa solver is validated and found capable of solving incompressible flow problems.

<sup>6</sup> Figure obtained from the paper of Jayaraju et al. (2007), (Figure 8.7(a) on p 152)

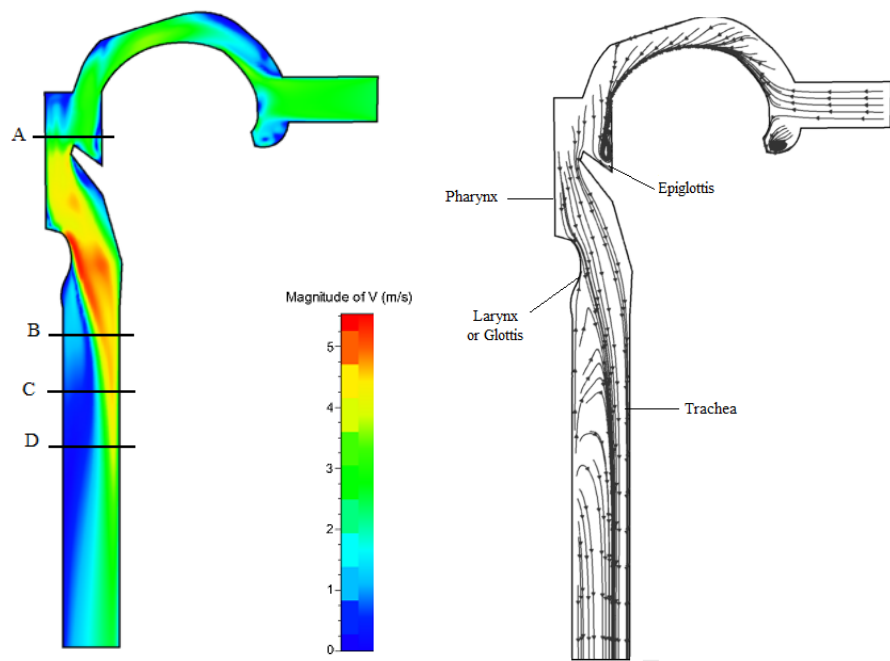


Figure 7.5: (left) Locations of the various cutting planes, (right) Velocity vector lines and nomenclature for the result of 30 l/min

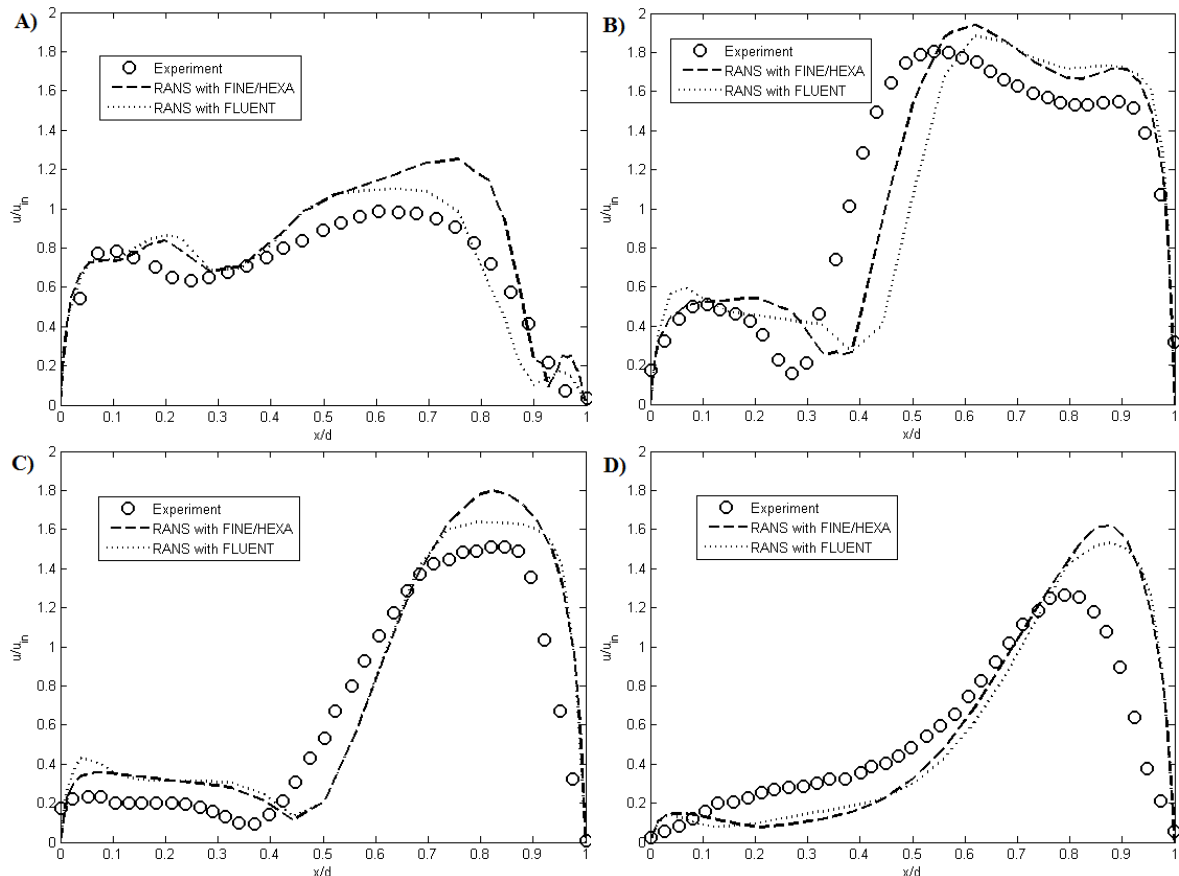


Figure 7.6: Comparison of experimental with RANS results obtained at the locations: (A) Five millimeters above epiglottis; (B,C,D) One, two and three tracheal diameters downstream of the larynx respectively.

## 8. Results application II: The realistic geometry

In this chapter the various results for the realistic geometry are given and discussed. This is done for the full geometry (Section 8.2) as well as for same the geometry with subsequent lung lobes removed (Section 8.3). The latter simulations are performed in order to simulate a surgical intervention. Flow quantities such as pressure, mass flow and airway resistance are computed for the different geometries. Due to the complexity of the geometry, the presentation of the results is, however, not straightforward. For this reason a separate chapter is dedicated towards the visualization of the results (Section 8.1). Unfortunately, unlike for the simplified geometry, there are no experimental results available yet for the current realistic CT-scan derived geometry. In order to give somewhat of an experimental validation the results are compared with results obtained by De Geeter (2010), who performed computations on the same geometry with the aid of the commercial software Fluent (Ansys). In the paper of De Geeter (2010), however, use is made of a fully tetrahedral mesh with about 4,000,000 cells for the simulations. Whenever possible, though, also a comparison is made with other studies.

### 8.1. Visualization of the results

It must be noticed that visualizing results with respect to the complex lung geometry is not straightforward. For this reason a selection of cutting planes is made with the aim of adequately capturing the results.

The first cut is made in the central sagittal plane, containing the laryngeal jet (see also Figure 3.2), and is used to visualize the velocity magnitude and turbulent kinetic energy contours in the middle of the trachea. Furthermore, several cutting planes are made along a selected pathway in each lung lobe. This is done in the following sequence: Two cutting planes are made at each subsequent bifurcation, one at the entrance, just before it splits up, and one at the exit, just before the next bifurcation (see the black lines corresponding to cutting planes in Figure 8.1, 8.2 and 8.3).

Using these pathways it is possible to reconstruct a measure of the mass flow, pressure and resistance in each lung lobe. Keep in mind that the number of bifurcation sections is different for each path (and each lung lobe).

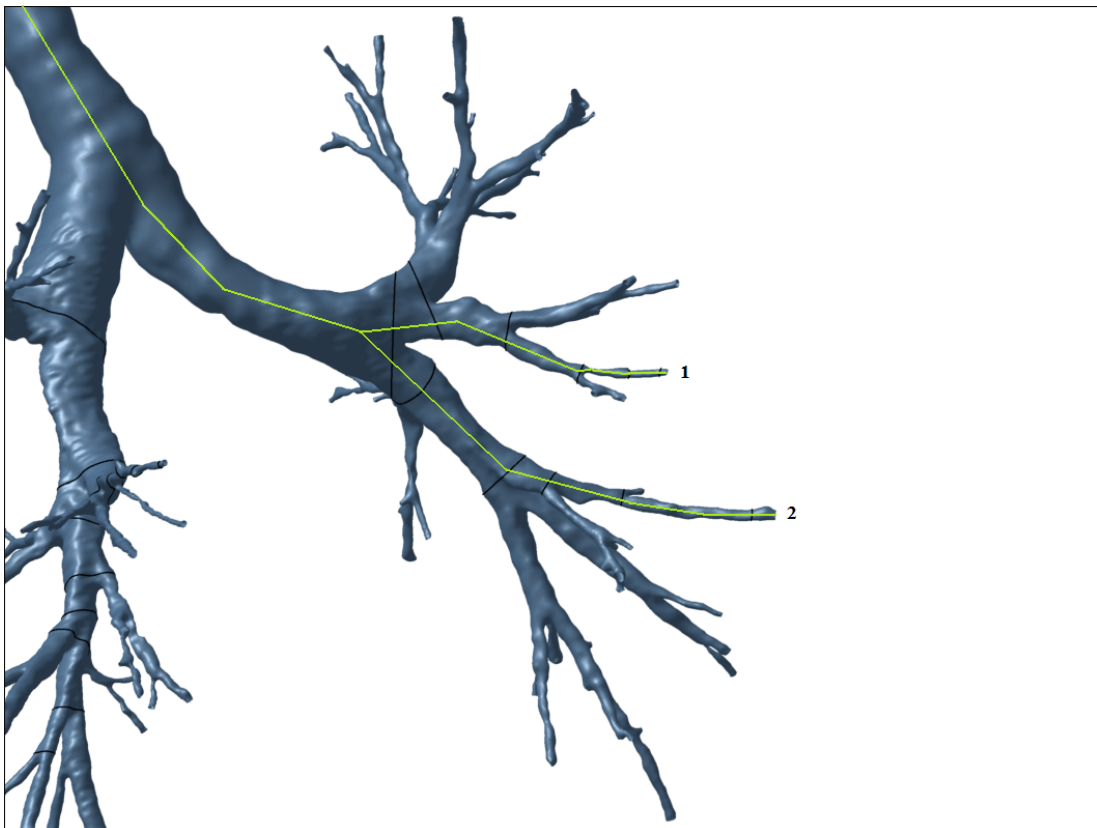


Figure 8.1: Selected lung lobe paths for (1) the LUL and (2) the LLL

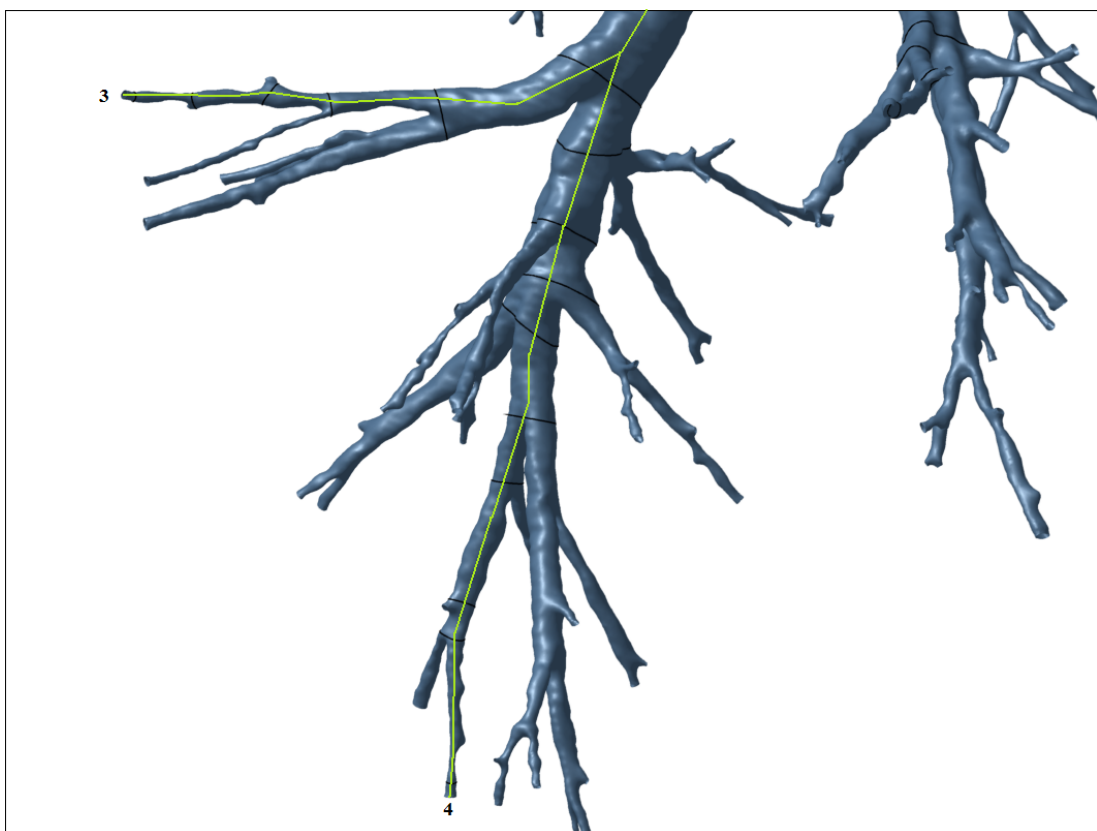


Figure 8.2: Selected lung lobe paths for (3) the RML and (4) the RLL



Figure 8.3: Selected lung lobe path for (5) the RUL

## 8.2. Full geometry

### 8.2.1. Velocity

For the visualization of the velocity magnitude contour a cut is made in the central saggital plane (see also Figure 3.2). The results for the three breathing rates of 15, 30 and 60 liter/min are shown below in Figure 8.4, 8.5 and 8.6. The values for the velocity magnitude are normalized with the inlet velocity to obtain a better comparison. Also to achieve more insight into the flow physics, the geometry was cut at four planes normal to the central saggital plane, as depicted in Figure 8.7 which also shows the velocity vector lines. At the crossing of these planes with the central plane, four velocity profiles are extracted for the different breathing rates (Figure 8.9).

First the most distinct flow features are discussed using the results for the case of normal breathing at 30 l/min. As can be seen, the flow enters through the mouthpiece and comes into the mouth cavity. From here on it accelerates due to the increased reduction of cross-sectional area. Because of the complexity of the lung geometry there are many recirculation zones, as can be seen in the right part of Figure 8.7. For example, the recirculation zone just after the mouthpiece and before the tongue. From the end of the mouth region the air flows in the pharynx, which is followed by a huge restriction in airway passage. This has the effect that the flow entering from the pharynx into the larynx has the form of a jet, the laryngeal jet. At this location due to a restriction in area, the velocity attains its peak value. Considering Figure 8.8(A), which is just before the laryngeal jet, one can see that the local maximum velocity is not in the middle of the cutting plane, as in most idealized geometries. Instead it is located towards the posterior side (A1 is depicted as anterior and A2 as the posterior side). This is also noticeable in Figure 8.8(C). Here the interior side shows two distinct vortices. From the different cross-sections also the complex nature of the geometry is observed. The

laryngeal jet continues from the glottal region further downstream. As a consequence flow separation occurs at the anterior side of the trachea, as can be seen from the streak lines in the right part of Figure 8.7.

This behavior is also reported in various other studies. For example Zhang et al. (2002), who developed a simple but representative upper oral airway geometry, reported flow separation due to the abrupt geometric changes and the generation of an asymmetric laryngeal jet after the glottis. Moreover, Jayaraju et al. (2007), who did simulations on a truly realistic geometry, found similar flow behavior and concluded that the pharynx as well as the larynx should be considered as the key morphological factors affecting the flow characteristics.

The results for the different breathing rates, as given in the left part of Figure 8.4, 8.5 and 8.6, seem to be very similar. However, when looking at the glottis area, the laryngeal jet is shorter for 60 l/min as compared to 30 l/min and 15 l/min. It expands faster for 60 l/min and transfers more momentum to the flow downstream. The simplified geometry, as discussed in Chapter 7, predicted the same behavior. This trend is also observed by De Geeter (2010), by Corcoran et al. (2000) and other studies. Corcoran et al. (2000) performed a phase Doppler study of the laryngeal jet in a larynx/trachea cast (see also Section 2.1),

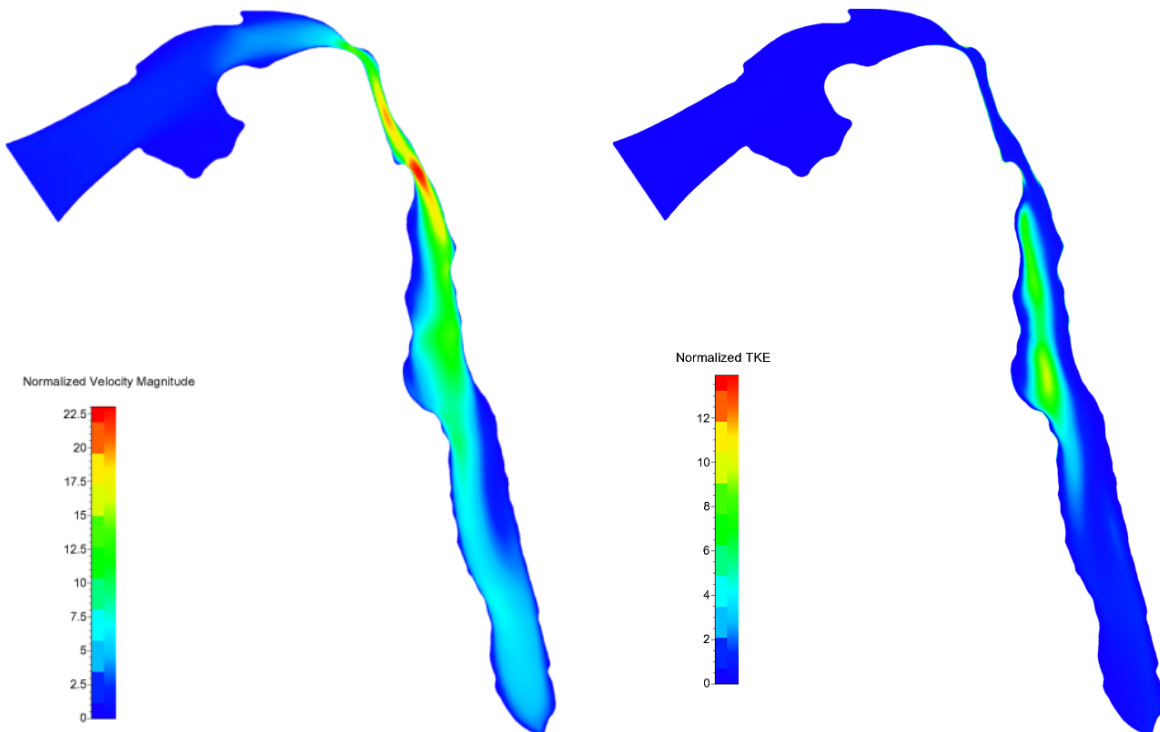


Figure 8.4: Results at the central saggital plane for 15 l/min: (left) Normalized velocity magnitude and (right) normalized turbulent kinetic energy

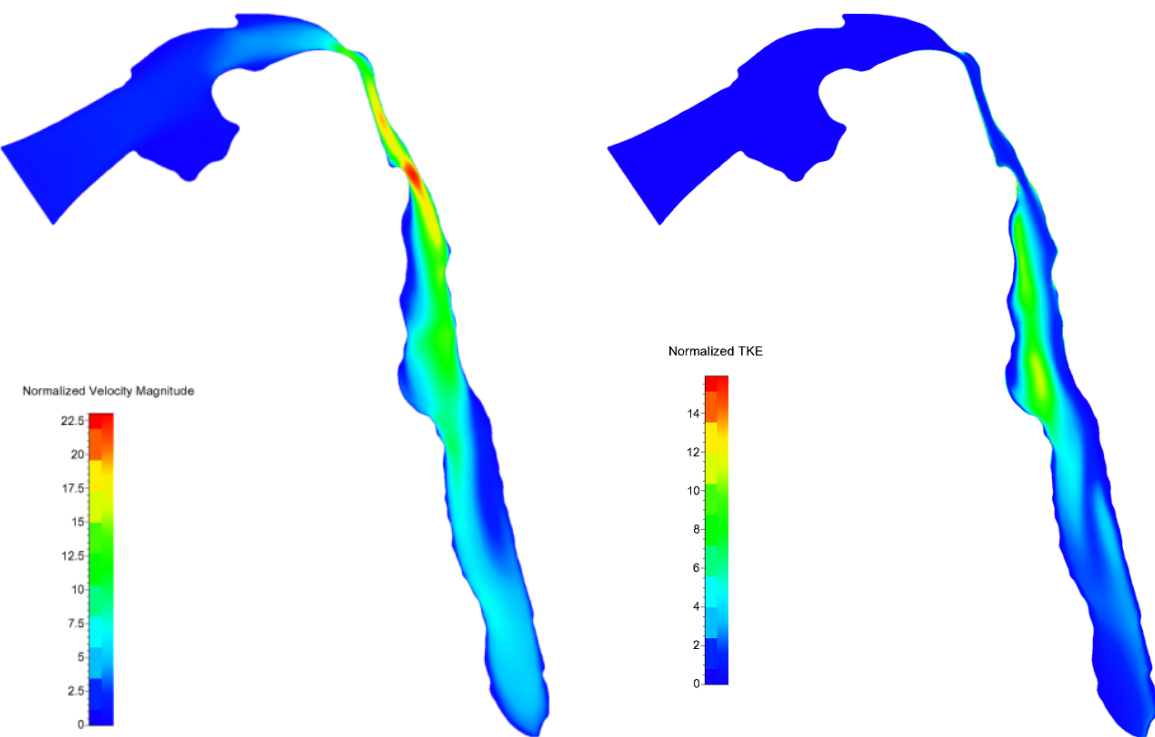


Figure 8.5: Results at the central saggital plane for 30 l/min: (left) Normalized velocity magnitude and (right) normalized turbulent kinetic energy

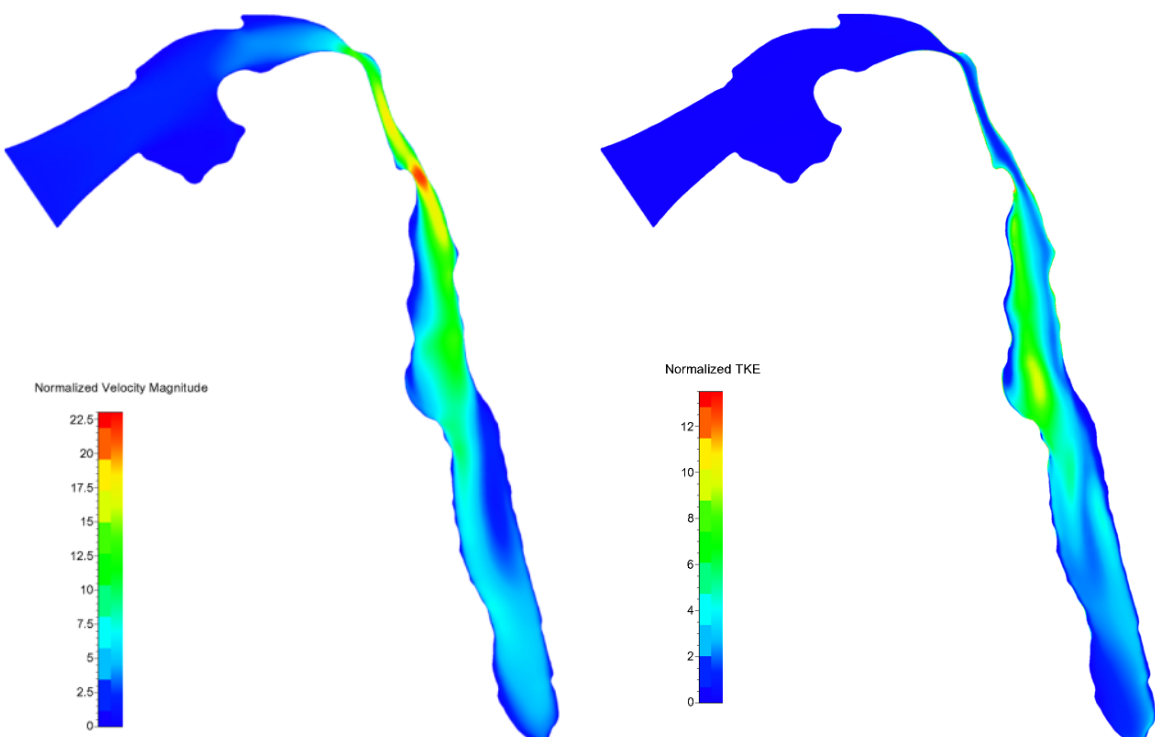


Figure 8.6: Results at the central saggital plane for 60 l/min: (left) Normalized velocity magnitude and (right) normalized turbulent kinetic energy

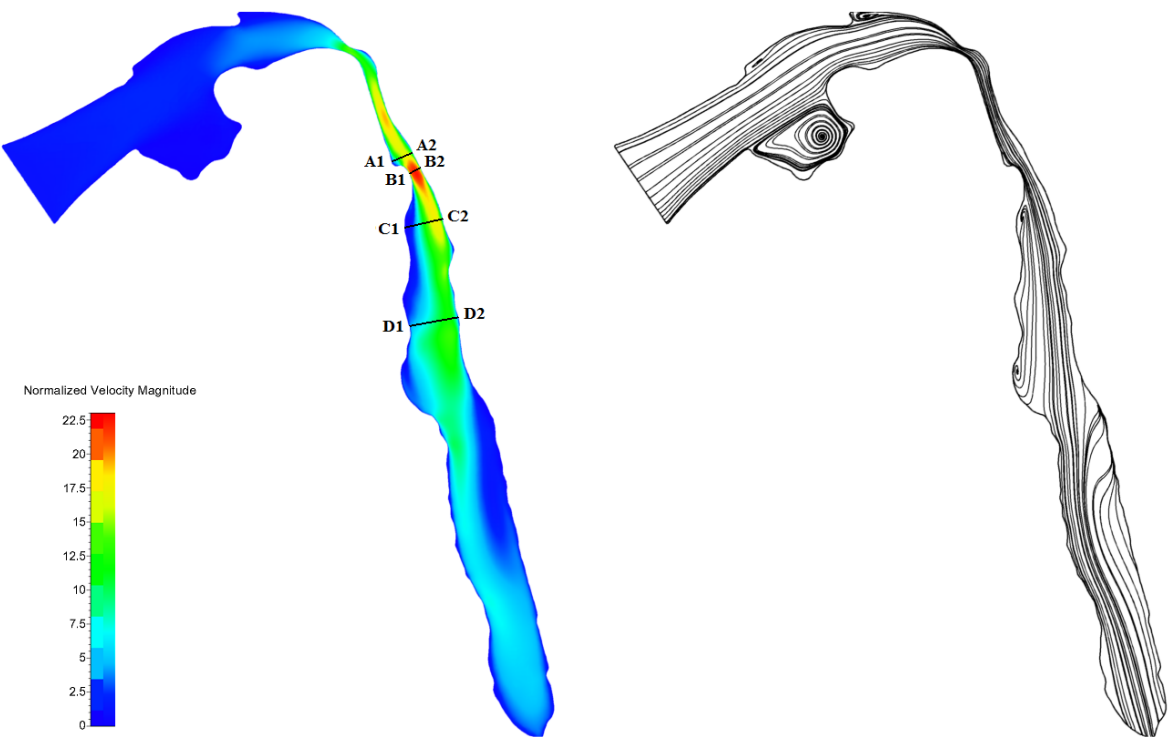


Figure 8.7: Results at the central saggital plane for 30 l/min: (left) Location of cutting planes, (right) Velocity vector lines

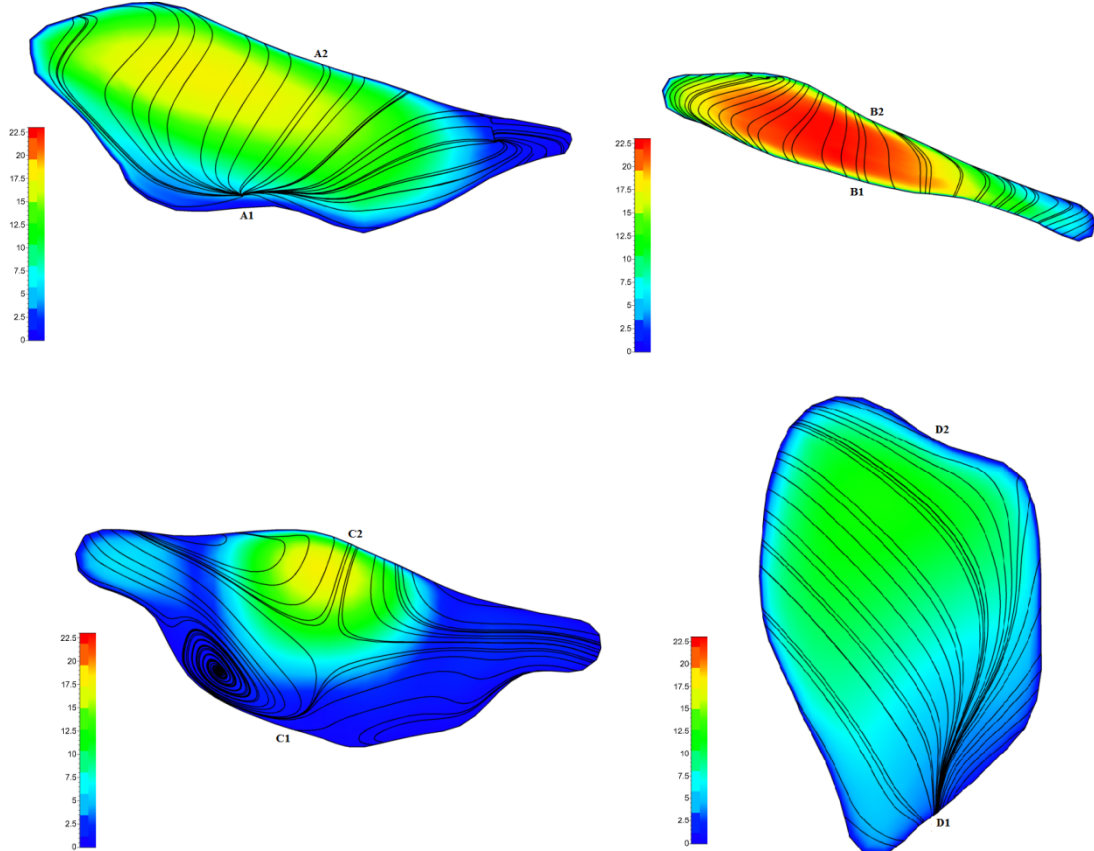


Figure 8.8: Cutting planes taken at four locations, corresponding to the left part of Figure 8.7, in the upper realistic geometry, where 1 depicts the posterior and 2 the anterior side

The four extracted normalized velocity profiles as shown in Figure 8.9 exhibit similar behavior. It is observed that for an increased inlet velocity, the normalized velocity profile decreases somewhat at the peak value. Moreover, for 60 l/min the velocity curve is going faster towards a uniform profile, as can be seen in part (C) and (D). Notice also that the velocity peak values in parts (A), (C) and (D) lie toward the posterior side of the geometry, while in part (B) the profile is almost uniform. De Geeter (2010) also made cuts at similar locations in the geometry and observed the same behavior, but in an even more pronounced way.

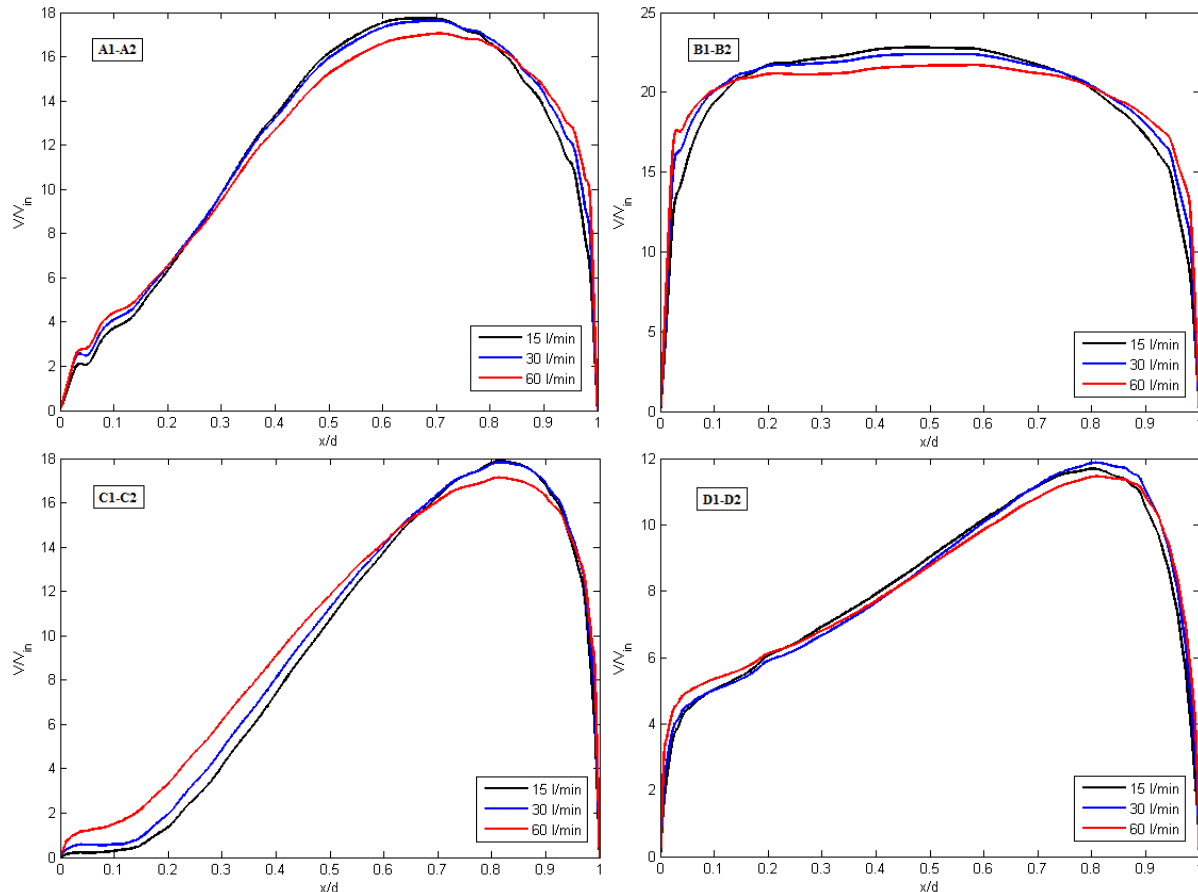


Figure 8.9: Velocity profiles extracted at four locations in the central saggital plane corresponding to the left part of Figure 8.7 for the different breathing rates

### 8.2.2. Turbulent kinetic energy

The results obtained for the normalized turbulent kinetic energy are shown in the right part of Figure 8.4, 8.5 and 8.6. The plots show transition to turbulence soon after the glottis region. This is also observed by various other papers, including Jayaraju et al. (2007), who concluded that the degree of turbulence critically depends on the degree of geometrical complexity of the extrathoracic airway model. Furthermore, when comparing the results, one notices that with increasing flow rate (going from 15 l/min to 60 l/min), the amount of turbulence increases. This is logic as with an increase in velocity, the Reynolds number increases and thus the flow becomes more dominantly turbulent.

### 8.2.3. Pressure

In Figure 8.10 the drop of total pressure is depicted for the case of 30 l/min. It can be seen from the contour plot how the pressure gradually decreases down the tracheobronchial tree with respect to the inlet section.

In the series of Figure 8.11 the pressure drop at each lung lobe is portrayed schematically, following the selected pathways as given in Section 8.1. The term pressure drop is here expressed as  $P - P_{in}$ , which gives a better overview of how the total pressure decreases following the selected lung path. It must be noted that in Figure 8.11 the values for the pressure are given starting from the first bifurcation of each subsequent lung lobe and not from the trachea or mouth. Comparing these plots, it can be noticed that the shape of the curves remains almost fixed. It is the total pressure that decreases with an increased breathing rate. These results are also consistent with the ones obtained by De Geeter (2010).

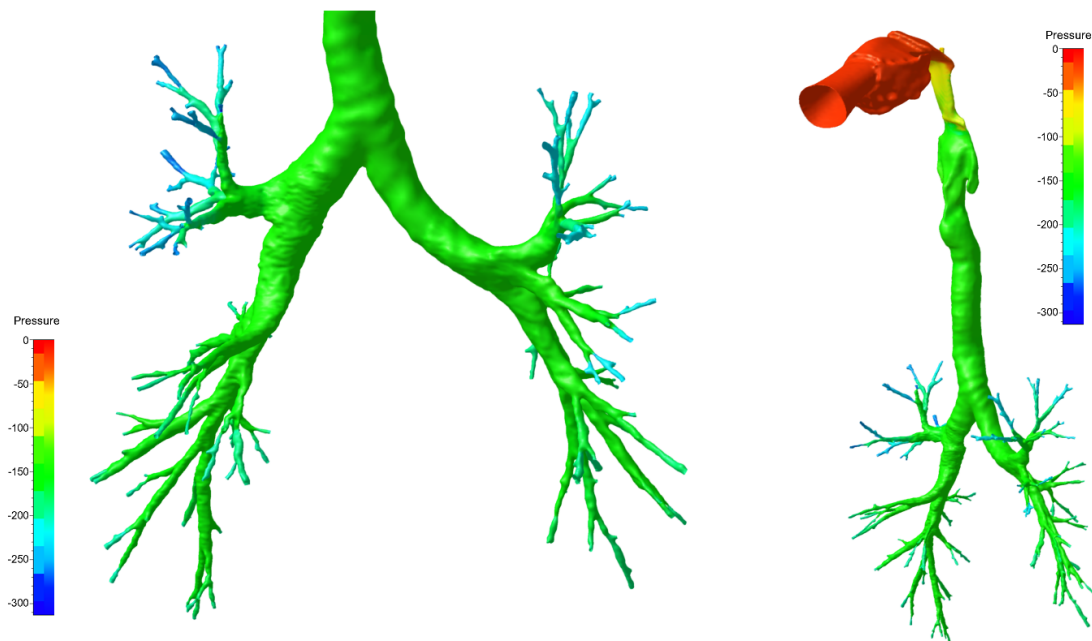


Figure 8.10: Global pressure drop for the case of 30 l/min

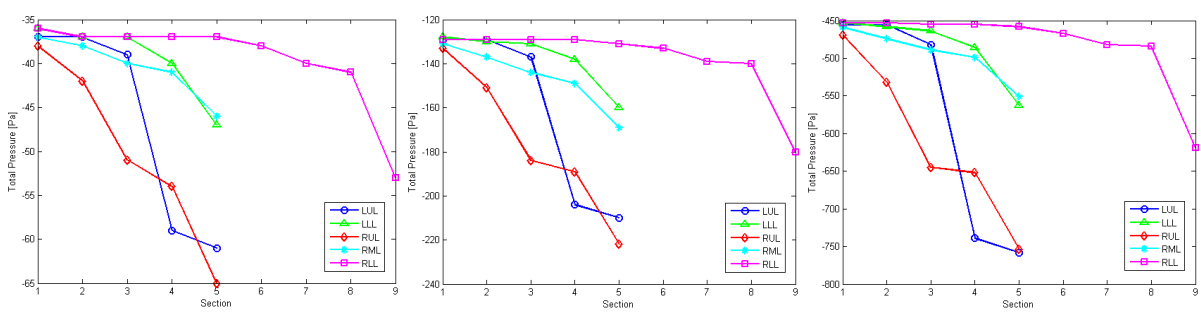


Figure 8.11: Pressure drop in the different lobe pathways for (left) 15 l/min, (middle) 30 l/min and (right) 60 l/min

Moreover, a comparison with the literature is offered. Beginning from the trachea till the end of each lung path (outlet), the values for the pressure drop are given in Table 8.1 for an inlet flow rate of 30 l/min.

Pathway	Pressure drop
LUL	82 Pa
LLL	32 Pa
RUL	94 Pa
RML	41 Pa
RLL	52 Pa
Average	60.2 Pa

Table 8.1: Average pressure drop along the pathways

The pressure drop seems to vary somewhat depending on the selected pathway. The higher pressure drops in the LUL and RUL can be explained as a result of the higher mass fractions in these lobes compared to the other lobes (see also section 8.3.1).

From Table 8.1 an average pressure drop of 60.2 Pa is obtained from the simulations, which is in accordance with the literature. For example Gemci et al. (2007) performed simulations at various inhalation flow rates. For the case of 30 l/min they indicated a pressure drop of 54 Pa following a pathway over a span of 17 generation airways. They used an inflow boundary condition at the trachea and an outflow boundary conditions at all terminal bronchi exits (in total 720 outlets for their digital reference lung model). Moreover, in the past Pedley et al. (Pedley, et al., 1971) and Pedley (Pedley, 1977) determined the pressure variation along the airway tree based on the energy equation. It was predicted as 60 Pa along Weibel's symmetric bronchial tree at a normal breathing rate. They also observed that local pressure drops are different because of anatomical asymmetries, as can be clearly seen in this thesis. Furthermore, when making this comparison one has to keep in mind that the present realistic geometry is state of the art and simulations in the past were always on idealized or simplified models and didn't yet include important geometric complexities.

## 8.2.4. Resistance

Airway resistance is the obstruction of the tracheobronchial tree to the air flow caused by friction forces. For an airway, group of airways or the whole lung the airway resistance is defined, in analogy with the resistance in an electrical network:

$$R = \frac{\Delta P}{\dot{m}} \quad (8.1)$$

Here Ohm's law is applied to the selected pathways, where  $\Delta P$  signifies the pressure difference over the bifurcation section and  $\dot{m}$  the mass flow rate in that section. Looking at the results as depicted in the left part of Figure 8.12, 8.13 and 8.14, it is noticeable that the shape of the curves remains the same, while the values of the airway resistance increase with increased flow rate. Furthermore, a huge peak in resistance occurs at the last bifurcation section of the RLL. The explanation is that the mass flow suddenly drops very steeply, while the pressure remains fixed. This is due to a junction with a much wider branch just before this bifurcation section. The largest part of the airflow will thus flow through the wider branch, leaving only a small portion of mass flow in our selected bifurcation section.

Moreover, De Geeter (2010) obtained similar results with their simulations for the different breathing rates, as shown in the right part of Figure 8.12, 8.13 and 8.14. These results are plotted next to results of this paper, in order to give a clear comparison. It must be noted that in this paper the same pathways are used with the exception of not including the trachea. It can be stated that both series of results exhibit the same behavior. The peak value for the LUL at the fourth bifurcation section in both results is visible. Furthermore, the peak value for the last section of the RLL is as well noticeable although with a slight reduction in peak. The values for the airway resistance are different, however.

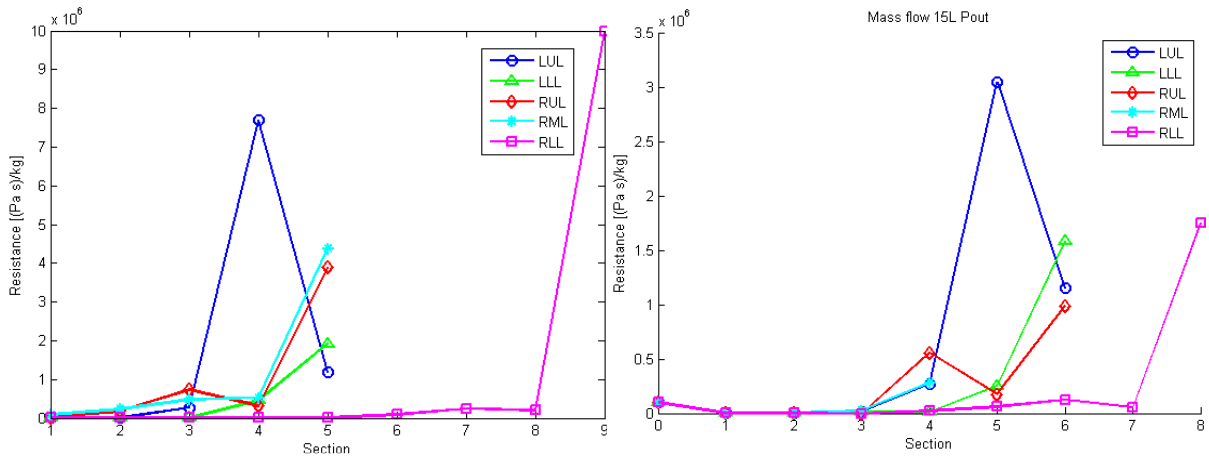


Figure 8.12: Resistance of the different lobe pathways for 15 l/min for results of (left) the present thesis with Fine/Hexa; (right) De Geeter (2010) with Fluent

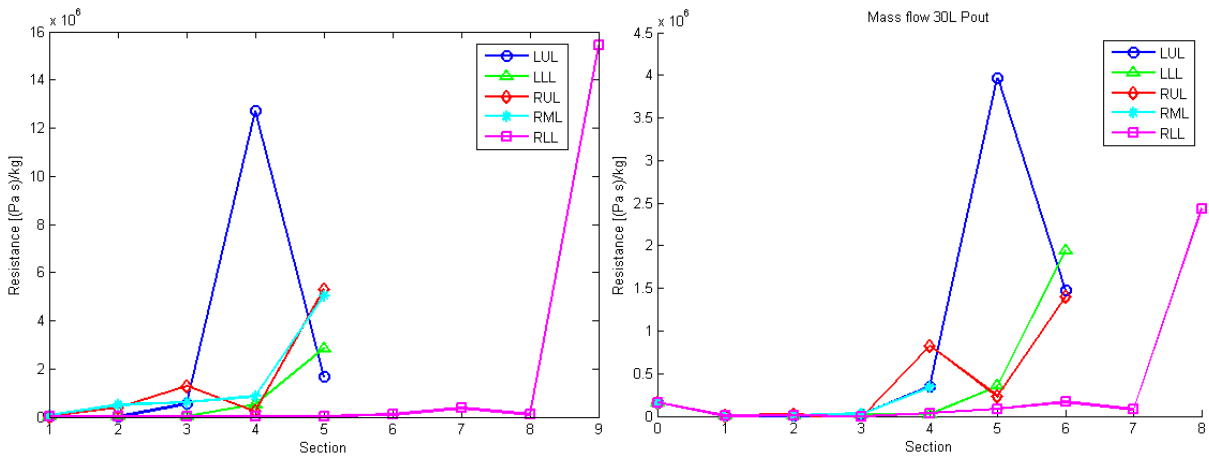


Figure 8.13: Results for the resistance of different lobe pathways for 30 l/min for results of (left) the present thesis with Fine/Hexa; (right) De Geeter (2010) with Fluent

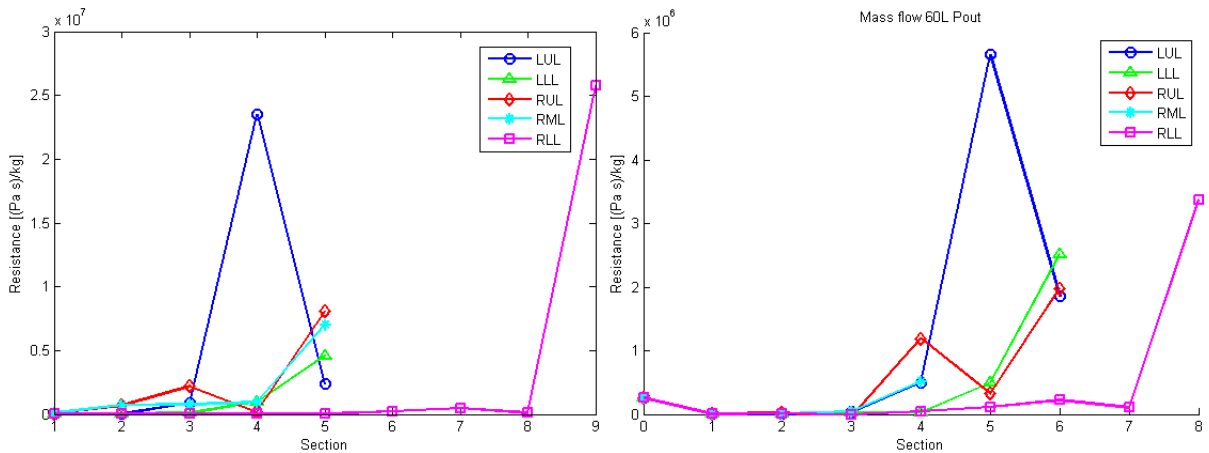


Figure 8.14: Results for the resistance of different lobe pathways for 60 l/min for results of (left) the present thesis with Fine/Hexa; (right) De Geeter (2010) with Fluent

### 8.3. Geometry with lungs removed

The same simulation is performed, however, now subsequently each lung lobe is removed from the geometry (see for example Figure 8.15). These results are important, because they will provide information about the internal flow phenomena after removing a lung lobe. In order to reduce the

amount of work, all following results are obtained for an inlet mass flow of 30 l/min for the flow simulation.

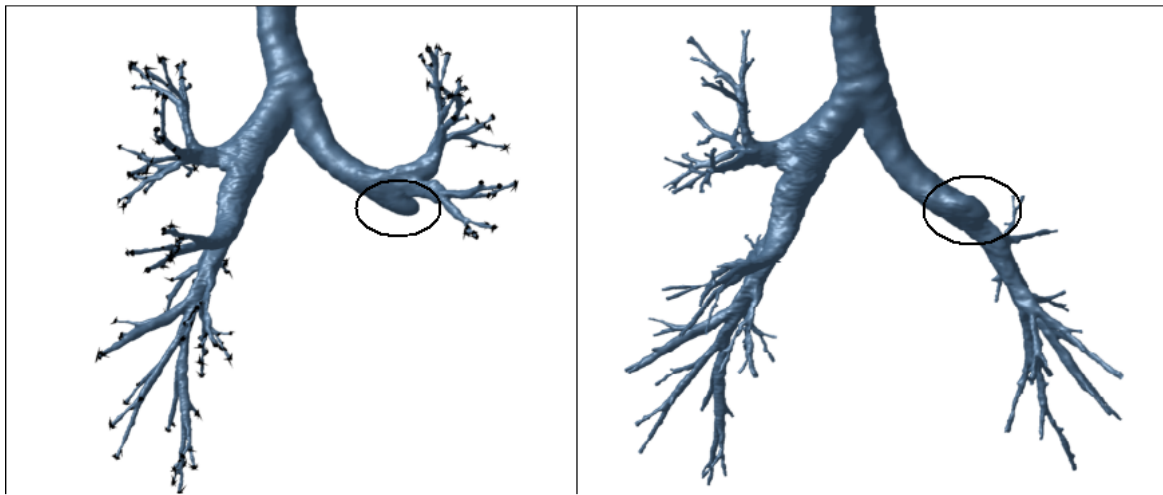


Figure 8.15: Geometry with lobes removed; (left) LLL removed and (right) LUL removed

### 8.3.1. Mass fractions

First the mass fractions are considered. In the upper left part of Figure 8.16, the mass flow in the different lung lobes of the full lung is portrayed. When a lung lobe is removed, all air goes to the remaining lobes. This can be seen in the increase of mass flow in each lung lobe compared with the full lung. One notices also that the shape of different curves remains unchanged after lobe removal. In the lower middle part of Figure 8.16, depicting the RML removal, the graph remains almost unchanged. This is because the RML only has a small share in the total lung volume, which can also be seen from Table 8.2.

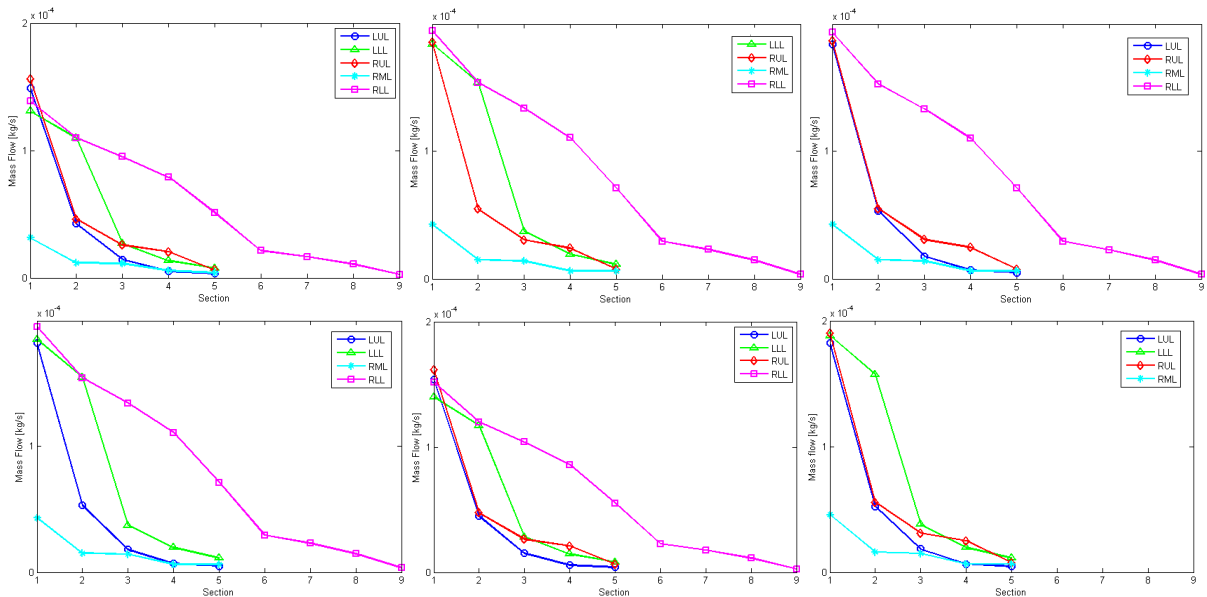


Figure 8.16: Mass flow in the different pathways for: Upper (left) the full lung, (middle) LUL removed and (right) LLL removed; and Lower (left) RUL removed, (middle) RML removed and (right) RLL removed

A more quantitative comparison is given in Table 8.2 and 8.3, where the different mass fractions,  $m/m_{in}$  are listed together. Also given is the increase in mass fraction when a subsequent lung lobe is

removed. The second column with the term 'full lung' contains the original mass fraction distribution of the entire lung. The RUL and LUL are the lobes which contain the largest mass fractions. Furthermore, when for example the RUL is removed, one sees an increase in mass fraction towards the left lung, but also inside the right lung the air is divided between its surviving lobes. As already mentioned, the RML contains only a small mass fraction of 5.15% and consequently when removed there will flow only a small percentage to the other lobes.

It is difficult to derive a global trend from this table. Nevertheless, the obtained results will be compared with those from the paper of De Geeter (2010) in order to try establishing a trend. The results of the latter one are given in Table 8.4. Notice that in this paper only simulations are performed for the case when the LUL and the LLL are removed. Also the mass fractions of the different lung lobes differ somewhat between the two studies with a maximum of 0.92%. With this in mind it is more appropriate to compare the increase in mass fraction. At first notice the trends seem to agree. When the LLL is removed most of the mass flow goes to the RLL, seconded by the LUL. This is also the case when the LUL is removed. Here most of the air goes again to the RLL, followed by the remaining left lung lobe. In both studies the RML acquires the lowest amount of air followed by the RUL.

Section	Full Lung			RUL removed		RML removed		RLL removed	
	$\dot{m}/\dot{m}_{in}$	$\dot{m}/\dot{m}_{in}$	Increase	$\dot{m}/\dot{m}_{in}$	Increase	$\dot{m}/\dot{m}_{in}$	Increase	$\dot{m}/\dot{m}_{in}$	Increase
Left Lung	45.59%	59.78%	+14.19%	47.84%	+2.25%	60.32%	+14.73%		
LUL	24.28%	29.66%	+5.38%	25.1%	0.82%	29.73%	+5.45%		
LLL	21.31%	30.12%	+8.81%	22.74%	1.43%	30.59%	+9.28%		
Right Lung	53.3%	38.98%	-14.32%	51.22%	-2.08%	38.55%	-14.75%		
RUL	25.51%	-	-	26.43%	+0.92%	31.08%	+5.57%		
RML	5.15%	7.05%	+1.9%	-	-	7.47%	+2.32%		
RLL	22.64%	31.93%	+9.29%	24.79%	+2.15%	-	-		

Table 8.2: Mass fractions of the different lung lobes for the case of RUL, RML and RLL subsequently removed

Section	Full Lung			LUL removed		LLL removed	
	$\dot{m}/\dot{m}_{in}$	$\dot{m}/\dot{m}_{in}$	Increase	$\dot{m}/\dot{m}_{in}$	Increase	$\dot{m}/\dot{m}_{in}$	Increase
Left Lung	45.59%	29.98%	-15.61%	29.98%	-15.61%		
LUL	24.28%	-	-	29.98%	+5.7%		
LLL	21.31%	29.98%	+8.67%	-	-		
Right Lung	53.3%	69.14%	+15.84	69.14%	+15.84%		
RUL	25.51%	30.34%	+4.83%	30.55%	+5.04%		
RML	5.15%	6.98%	+1.83%	6.99%	+1.84%		
RLL	22.64%	31.82%	+9.18%	31.6%	+8.96%		

Table 8.3: Mass fractions of the different lung lobes for the case of LUL and LLL subsequently removed

Section	Full Lung			LUL removed		LLL removed	
	$\dot{m}/\dot{m}_{in}$	$\dot{m}/\dot{m}_{in}$	Increase	$\dot{m}/\dot{m}_{in}$	Increase	$\dot{m}/\dot{m}_{in}$	Increase
Left Lung	47.3%	32.6%	-14.7%	33.0%	-14.3%		
LUL	25.2%	-	-	33.0%	+7.8%		
LLL	22.1%	32.6%	10.5%	-	-		
Right Lung	52.7%	68.4%	+15.7%	67.0%	+13.9%		
RUL	25.8%	29.2%	+3.4%	29.1%	+3.3%		
RML	4.5%	6.9%	+2.4%	6.8%	+2.3%		
RLL	22.4%	32.3%	+9.9%	31.1%	+8.9%		

Table 8.4: Mass fractions obtained by De Geeter (2010) for the case of LUL and LLL removed

### 8.3.2. Pressure

In Figure 8.17 the total pressure is considered for the different geometries with lobes removed. It is noticed that when a subsequent lung lobe is removed the total pressure for the remaining lobes drops with about  $\sim 20$  Pa. This is the result of forcing air through a reduced area, hereby increasing velocity and decreasing total pressure. It is striking that when the LUL or LLL is removed (see upper middle and right part of Figure 8.17) the pressure distribution in the right lobe remains almost unchanged. This is also noticed by De Geeter (2010). The same unchanged total pressure can be seen in the left lung, when the RLL and RUL are removed. When the RML is removed, however, the shape of the pressure curves for the other lobes remains unchanged with respect to the full lung. The reason for this, which was already stated, is that the RML contains only a small amount of mass fraction. And consequently when removed there is only a small amount of air that needs to be distributed.

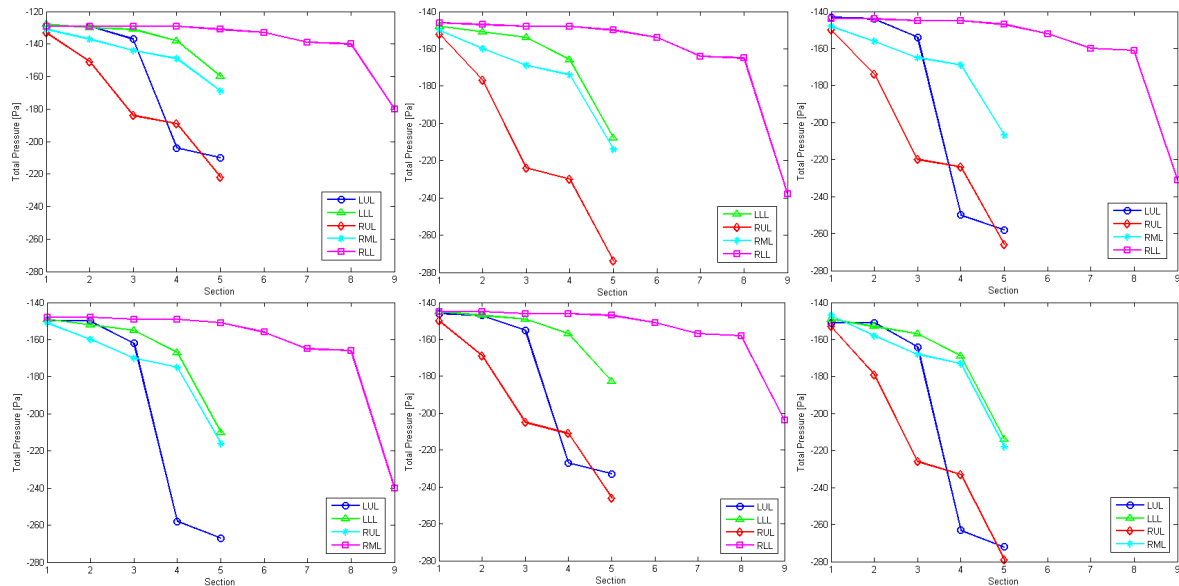


Figure 8.17: Pressure drop in the different pathways for: Upper (left) the full lung, (middle) LUL removed and (right) LLL removed; and Lower (left) RUL removed, (middle) RML removed and (right) RLL removed

## 8.4. Conclusion

Considering the results for the full geometry, the diverse simulated flow features including flow separation, recirculation zones and location of peak velocity and turbulence are found to concur with the literature. The length of the laryngeal jet is noticed to decrease with increasing flow rate. The average pressure drop over the tracheobronchial tree is simulated to be about  $\sim 60$  Pa for an inhalation rate of 30 l/min, which is in very good agreement with various papers. Furthermore, airway resistance is seen to increase when going down the tracheobronchial tree, i.e. when the airway branch diameter decreases.

Results for the simulations on the geometries subjected to surgical intervention show that when a subsequent lung lobe is removed the air is redistributed amongst the remaining lobes and the total pressure drops about  $\sim 20$  Pa. Keep in mind that caution needs to be taken because no direct experimental results are available at the moment to compare with.

## 9. Results application III: Software comparison

In this chapter a software comparison is offered between the solver of Fine/Hexa and Fluent. It must be noted that unlike Fine/Hexa, Fluent offers both a compressible and incompressible solver.

For the comparison the mesh of 5,230,000 cells is run with the Fluent solver using the same computational parameters as previously set with Fine/Hexa for a normal breathing rate of 30 l/min.

The results at the different lung lobe paths (as defined in Section 8.1) are given in Figure 9.1, 9.2 and 9.3 respectively for the mass flow rate, the pressure drop and the airway resistance. The results for the mass flow rate are in good agreement and show virtually almost no difference. Regarding the pressure drop in Figure 9.2 and the airway resistance in Figure 9.3, it is noticed that the general curve trends seem to agree. The values for both pressure drop and resistance agree up to the third bifurcation section. After this section they differ somewhat. A reason for this can be the fact that the pressure at the outlets has to be iteratively changed to match the required lung lobe mass fraction conditions (see also section 5.3). In this fashion the values for the pressure at the different outlets changes somewhat between both solvers.

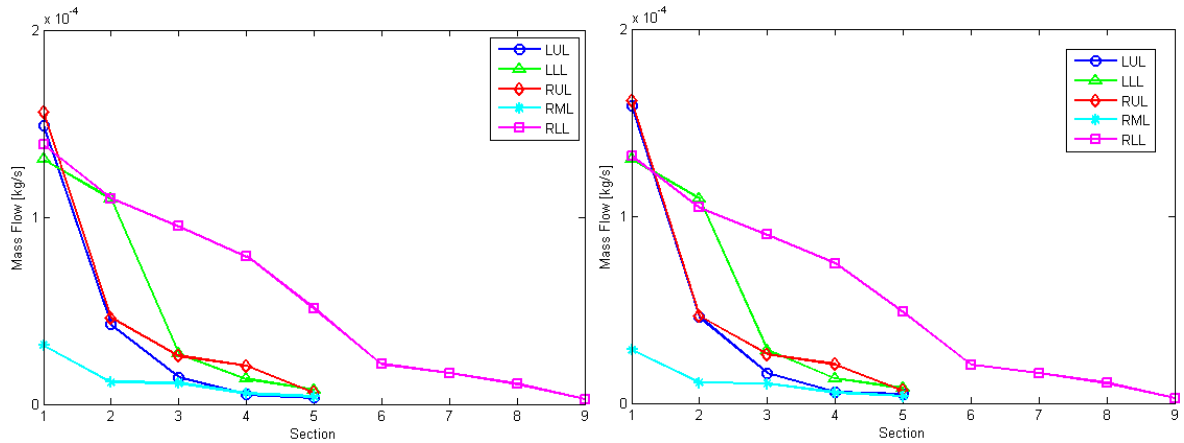


Figure 9.1: Mass flow rate obtained with: (left) Fine/Hexa; (right): Fluent

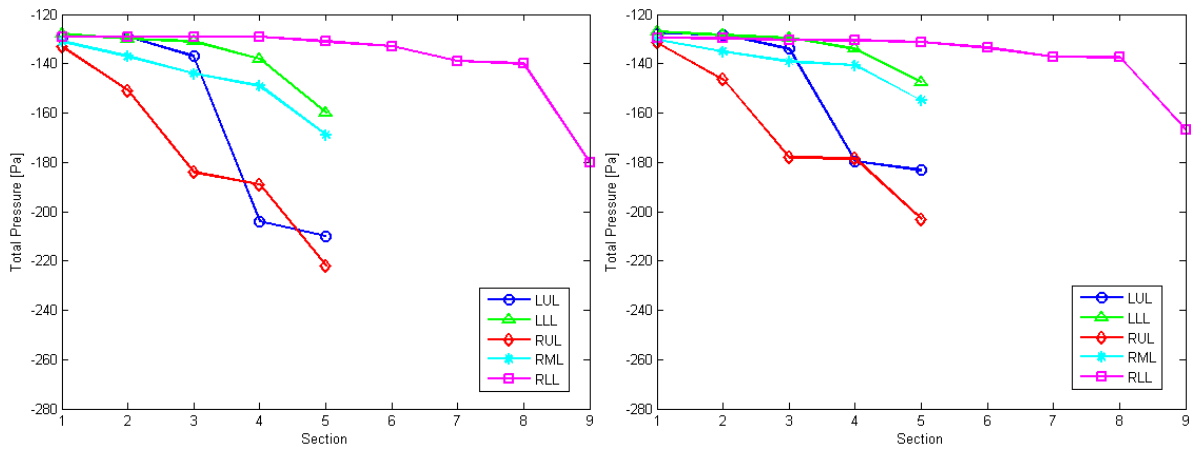


Figure 9.2: Pressure drop obtained with: (left) Fine/Hexa; (right): Fluent

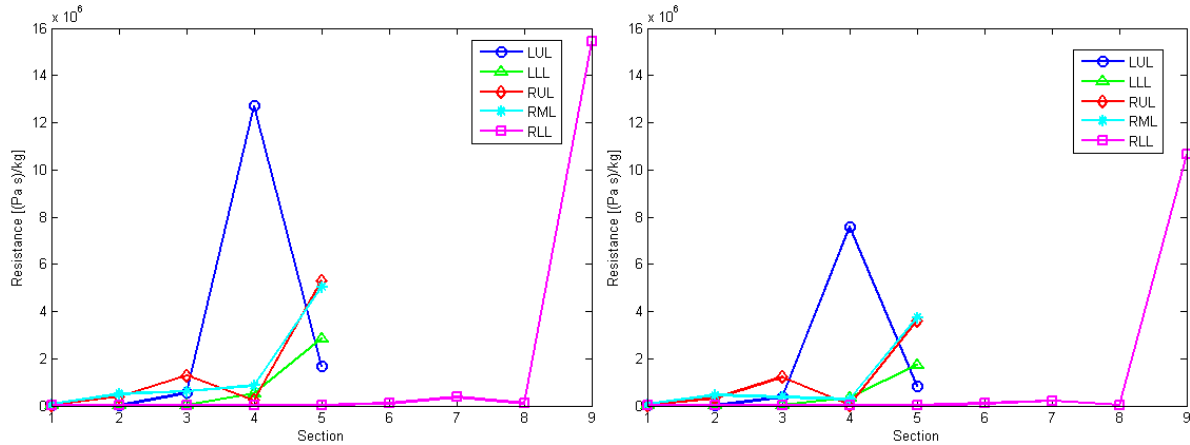


Figure 9.3: Airway resistance obtained with: (left) Fine/Hexa; (right): Fluent

Moreover, in order to make a choice between solvers, a comparison in computational time is offered in Table 9.1. For this purpose the mesh of 5,230,000 cells is run with both solvers for 1500 iterations on six Intel Xeon x5560 2.8 MHz quad-core processors. Keep in mind that within the Fine/Hexa solver standard four levels of multigrid are applied to speed up convergence.

	Fluent	Fine/Hexa
Wall time	0h43min	1h06min
Total CPU time	4h 59min	13h 56min

Table 9.1: Total CPU and wall time after 1500 iterations for both solvers

Considering the results in Table 9.1, it can be stated that using the Fluent solver saves about 9 hours of computation time compared to Fine/Hexa solver. Also in computing the wall distances, the Fluent solver is seen to be 23 minutes faster. The reason that Fluent is more time effective lies in the fact that it is an incompressible solver and for example does not solve for the energy equation. Whereas Fine/Hexa is a compressible solver, which automatically solves the energy equation (thus one equation more). Furthermore, the Fine/Hexa software requires fine-tuning of the preconditioning parameters in order to solve for incompressible flow problems. This is also considered time consuming and less user friendly.

In conclusion, both solvers produce almost identical results. However, when regarding the computational time, it can be concluded that with the Fluent solver the solution converges about 2.8 times faster. Fluent is also considered to be more user friendly.

## 10. Conclusions and recommendations

The present thesis offers a mesh independent study and shows that it is possible to have a mesh independent solution on a truly realistic lung geometry, as extracted from CT scan data. As a result a mesh of 5,230,000 computational cells was obtained for simulation purposes. Furthermore, a comparison is performed between two software's, namely Fine/Hexa and Fluent, to check which solver is more capable of performing simulations on the complex geometry. Both solvers have been seen to produce almost identical results. However, when considering the computational time, it is noticed that with Fluent the solution converges about 2.8 times faster. Thus the Fluent solver is considered more time effective and also more easier to use for performing computations on the realistic geometry.

In addition, various important flow phenomena have been simulated on the complex geometry and were seen to be in good accordance with the literature. Also, in order to work towards a software tool for aiding lung surgeons, computations have been performed on geometries with subsequent lung lobes removed. Various flow quantities such as pressure drop, mass flow rate and airway resistance have been looked at. Keep in mind that no direct experimental results are yet available and that caution needs to be taken.

If CFD will ever be able to produce an effective software aid and influence medical decisions, still a significant amount of work needs to be done. First of all experimental results need to be obtained for the realistic geometry in order to further validate the obtained computational results. Furthermore, considering the boundary conditions, some algorithm needs to be provided that automatically performs the iterative process to obtain pressure outlet boundary conditions from the given mass fractions. At the moment this is still too time consuming. It can also be interesting to compare between even more software's, such as openFOAM (OpenCFD Ltd, UK) or COOLFluid (VKI, Brussels, Belgium), in order to obtain an optimal software for this application.

Moreover, post-processing of the results needs to be greatly improved. At the moment it is still too difficult and time consuming because of the irregular, non-symmetric complex lung geometry and huge grid size.

In this way an effective CFD software tool will have to find a balance between providing a mesh independent solution on a realistic geometry extracted by means of CT scan or other techniques, running accurate simulations with patient specific boundary conditions and effectively post processing the results. And all of this in a reasonable time span to be able to help the patient.

## Bibliography

- Brouns M. [et al.]** Tracheal stenosis: A flow dynamics study. [Journal] // Journal of Applied Physiology. - 2007. - Vol. 102. - pp. 1178-1184.
- Calay R. K., Kurujareon J. and Holdo A. E.** Numerical simulation of respiratory flow patterns within the human lung [Journal] // Respiratory Physiology and Neurobiology. - 2002. - Vol. 130. - pp. 201-221.
- Cebral J. R. and Summer R. M.** Tracheal and central bronchial aerodynamics using virtual bronchoscopy and computational fluid dynamics [Journal] // IEEE Transactions on Medical Imaging. - 2004. - 8 : Vol. 23. - pp. 1021-1023.
- Cheng Y. S., Zhou Y. and Chen B. T.** Particle deposition in a cast of human oral airways [Journal] // Aerosol Science and Technology. - 1999. - Vol. 31. - pp. 286-300.
- Choi D. and Merkle C. L.** Prediction of channel and boundary-layer flows with a low-reynolds number turbulence model [Journal] // AIAA Journal. - 1985. - Vol. 23. - pp. 1518-1524.
- Comer J K, Kleinstreuer C and Zhang Z** Flow structures and particle deposition patterns in double-bifurcation airway models. Part 1: Air flow fields [Journal] // Journal of Fluid Mechanics. - 2001. - Vol. 435. - pp. 25-54.
- Corcoran T. E. and Chigier N.** Characterization of the laryngeal jet using phase doppler interferometry [Journal] // Journal of Aerosol Medicine. - 2000. - Vol. 13. - pp. 125-137.
- De Backer J. W. [et al.]** Flow analyses in the lower airways: Patient-specific model and boundary conditions [Journal] // Medical Engineering and Physics. - 2008. - Vol. 30. - pp. 872-879.
- De Backer Jan W. [et al.]** Novel imaging techniques using computer methods for the evaluation of the upper airway in patients with sleep-disordered breathing: A comprehensive review [Journal] // Sleep Medicine Reviews. - 2008. - Vol. 12. - pp. 437-447.
- De Geeter Kasper** CFD simulatie van stroming in realistische longgeometriën [Report] / VUB. - Brussels : Masterthesis, 2010.
- Finlay W H** The mechanics of inhaled pharmaceutical aerosols [Book]. - London, UK : Academic press, 2001.
- Gemci T [et al.]** A CFD study of the throat during aerosol drug delivery using heliox and air. [Journal] // Journal of Aerosol Science. - 2003. - Vol. 34. - pp. 1175-1192.
- Gemci T. [et al.]** Computational model of airflow in upper 17 generations of human respiratory tract [Journal] // Journal of Biomechanics. - 2008. - Vol. 41. - pp. 2047-2054.
- Hakimi Nouredine** Preconditioning methods for time dependent navier-stokes equations [Report] : Ph.D. Thesis / Fluid Mechanics ; VUB. - Brussels : [s.n.], 1997.
- Heenan A F [et al.]** Experimental measurements and computational modeling of the flow field in an idealized human oropharynx. [Journal] // Experiments in Fluids. - 2003. - Vol. 35. - pp. 70-84.

**Hirsch C [et al.]** A multiblock/multigrid code for the efficient solution of complex 3D navier-stokes flows [Journal] // European symposium on aerodynamics for space vehicles. - 1991. - pp. 415-420.

**Hofmann W. and Balashazy I.** Particle deposition patterns within airway bifurcations - solution of the 3D Navier-Stokes equations [Journal] // Resp. Prot. Dosim.. - 1991. - Vol. 38. - pp. 57-63.

**Horsfield K. [et al.]** Models of the human bronchial tree [Journal] // Journal of Applied Physiology. - 1971. - Vol. 31. - pp. 207-217.

**Jameson A, Schmidt W and Turkel E** Numerical simulation of euler equations by finite volume methods using runge-kutta time stepping schemes [Journal] // AIAA Journal. - 1981. - pp. 81-1259.

**Jayaraju S. T. [et al.]** Fluid flow and particle deposition analysis in a realistic extrathoracic airway model using unstructured grids. [Journal] // Journal of Aerosol Science. - 2007. - Vol. 38. - pp. 494-508.

**Johnstone A. [et al.]** The flow inside a idealized form of the human extra-thoracic airway. [Journal] // Experiments in Fluids. - 2004. - Vol. 37. - pp. 673-689.

**Kalitzin Georgi [et al.]** Near-wall behavior of RANS turbulence models and implications for wall functions [Journal] // Journal of Computational Physics. - 2005. - Vol. 204. - pp. 265-291.

**Katz I M and Martonen T B** Flow patterns in a three-dimensional laryngeal model [Journal] // Journal of Aerosol Medicine / ed. 511. - 1996. - 4 : Vol. 9. - p. 501.

**Katz I M and Martonen T B** Three-dimensional computational study of inspiratory aerosol flow through the larynx: The effect of glottal aperture modulation [Journal] // Journal of Aerosol Science. - 1997. - 6 : Vol. 28. - pp. 1073-1083.

**Kleinstreuer C, Zhang Z and Kim C S** Combined inertial and gravitational deposition of microparticles in small model airways of a human respiratory system. [Journal] // Journal of Aerosol Science. - 2007. - Vol. 38. - pp. 1047-1061.

**Kriete A. [et al.]** Simulations at a newly derived reference model of the human lung [Journal] // Proceedings of SPIE. - 2004. - Vol. 5318. - pp. 163-169.

**Lambert A. [et al.]** Regional deposition of particles in an image-based airway model: large-eddy simulation and left-right lung ventilation asymmetry [Journal] // Aerosol Science and Technology. - 2010.

**Li Z, Kleinstreuer C and Zhang Z** Simulation of airflow fields and microparticle deposition in realistic human lung airway models. Part i: Airflow patterns [Journal] // European Journal of Mechanics B/Fluids. - 2007. - Vol. 26. - pp. 632-649.

**Li Z., Kleinstreuer C. and Zhang Z.** Simulation of airflow fields and microparticle deposition in realistic human lung airway models. Part i: Airflow patterns [Journal] // European Journal of Mechanics B/ Fluids. - 2007. - Vol. 26. - pp. 632-649.

**Lin Ching-Long [et al.]** Characteristics of the turbulent laryngeal jet and its effect on airflow in the human intra-thoracic airways [Journal] // *Respir. Physiol. Neurobiol.* . - 2007. - 2-3 : Vol. 157. - pp. 295-309.

**Liu Y, So R. M. C. and Zhang C. H.** Modeling the bifurcating flow in an asymmetrix human pulmonary airway [Journal] // *Journal of Biomechanics*. - 2003. - Vol. 36. - pp. 951-959.

**Longest P. W. and Vinchurkar S.** Effects of mesh style and grid convergence on particle deposition in bifurcating airway models with comparisons to experimental data [Journal] // *Medical Engineering and Physics*. - 2007a. - Vol. 29. - pp. 350-366.

**Longest P. Worth and Vinchurkar Samir** Effects of mesh style and grid convergence on particle deposition in bifurcating airway models with comparisons to experimental data [Journal] // *Medical Engineering and Physics*. - 2007. - Vol. 29. - pp. 350-366.

**Luo H. Y. and Liu Y.** Modeling the bifurcating flow in a CT-scanned human lung airway [Journal] // *Journal of Biomechanics*. - 2008. - Vol. 41. - pp. 2681-2688.

**Ma B. and Lutchen K. R.** An anatomically based hybrid computational model of the human lung and its application to low frequency oscillatory mechanics [Journal] // *Annals of Biomedical Engineering*. - 2006. - 11 : Vol. 34. - pp. 1691-1704.

**Martonen T B [et al.]** Three dimensional computer modeling of the human upper respiratory tract. [Journal] // *Cell. biochemistry and biophysics*. - 2001. - Vol. 35. - pp. 255-261.

**Menter F.** Two-equation eddy viscosity turbulence models for engineering applications [Journal] // *AIAA Journal*. - 1994. - Vol. 32. - pp. 1299-1310.

**Nowak Natalya, Kakade Prashant P. and Annapragada Ananth V.** Computational fluid dynamics simulation of airflow and aerosol deposition in human lungs [Journal] // *Annals of Biomedical Engineering*. - 2003. - Vol. 31. - pp. 373-390.

**Pedley T J, Schroter R C and Sudlow M F** Flow and pressure drop in systems of repeatedly branching tubes [Journal] // *Journal of Fluid Mechanics*. - 1971. - Vol. 46. - pp. 363-383.

**Pedley T. J.** Pulmonary fluid dynamics [Journal] // *Annual Review of Fluid Mechanics*. - 1977. - Vol. 9. - pp. 229-271.

**Renotte C, Bouffoux V and Wilquem F** Numerical 3D oscillatory flow in the time-varying laryngeal channel [Journal] // *Journal of Biomechanics*. - 2000. - Vol. 33. - pp. 1637-1644.

**Roache P.** Computational Fluid Dynamics [Book]. - Albuquerque : [s.n.], 1992.

**Schmidt A. [et al.]** A digital reference model of the human bronchial tree [Journal] // *Computerized Medical Imaging and Graphics*. - 2004. - Vol. 28. - pp. 203-211.

**Shi H., Kleinstreuer C. and Zhang Z.** Nanoparticle transport and deposition in bifurcating tubes with different inlet conditions [Journal] // *Physics of Fluids*. - 2004. - 7 : Vol. 16. - pp. 2199-2213.

**Stapleton K. W. [et al.]** ON the suitability of k - e turbulence modeling for aerosol deposition in the mouth and throat: A comparison with experiment [Journal] // Journal of Aerosol Science. - 2000. - Vol. 31. - pp. 739-749.

**Turkel E.** Preconditioning methods for solving the incompressible and low-speed compressible equations [Journal] // Journal of Computational Physics. - 1987. - Vol. 72. - pp. 277-298.

**van Ertbruggen C., Hirsch C. and Paiva M.** Anatomically based three-dimensional model of airways to simulate flow and particle transport using computational fluid dynamics [Journal] // Journal of Applied Physiology. - 2005. - 3 : Vol. 98. - pp. 970-980.

**Vos W [et al.]** Correlation between severity of sleep apnea and upper airway morphology based on advanced anatomical and functional imaging [Journal] // Journal Biomechanics. - 2007. - Vol. 40. - pp. 2207-2213.

**Weibel E. R.** Morphometry of the Human Lung [Book]. - Berlin : Springer, 1963.

**Wilcox D. C.** Turbulence modeling for CFD [Report] / DCW Industries, Inc. - California : [s.n.], 1998.

**Xi J. and Longest P W** Transport and deposition of micro-aerosols in realistic and simplified models of the oral airway. [Journal] // Annals of Biomedical Engineering. - 2007. - Vol. 35. - pp. 560-581.

**Yu G., Zhang Z. and Lessmann R.** Fluid flow and particle diffusion in the human upper respiratory system. [Journal] // Aerosol Science and Technology. - 1998. - Vol. 28. - pp. 146-158.

**Zhang Z. and Kleinstreuer C.** Airflow structures and nano-particle deposition in a human upper airway model [Journal] // Journal of Computational Physics. - 2004. - Vol. 198. - pp. 178-210.

**Zhang Z. and Kleinstreuer C.** Low-Reynolds-number turbulent flows in locally constricted conduits: A comparison study [Journal] // AIAA Journal. - 2003. - 5 : Vol. 41. - pp. 831-840.

**Zhang Z., Kleinstreuer C. and Kim C. S.** Micro-particle transport and deposition in a human oral airway model [Journal] // Journal of Aerosol Science. - 2002. - Vol. 33. - pp. 1635-1652.